



Marine cellular
cloudiness and
surface heat fluxes

J. Kazil et al.

On the interaction between marine boundary layer cellular cloudiness and surface heat fluxes

J. Kazil^{1,2}, G. Feingold², H. Wang³, and T. Yamaguchi^{1,2}

¹Cooperative Institute for Research in Environmental Sciences (CIRES), University of Colorado, Boulder, Colorado, USA

²Chemical Sciences Division, Earth System Research Laboratory, NOAA, Boulder, Colorado, USA

³Pacific Northwest National Laboratory, Richland, WA, USA

Received: 5 June 2013 – Accepted: 12 June 2013 – Published: 15 July 2013

Correspondence to: J. Kazil (jan.kazil@noaa.gov)

Published by Copernicus Publications on behalf of the European Geosciences Union.

Title Page

Abstract

Introduction

Conclusions

References

Tables

Figures



Back

Close

Full Screen / Esc

Printer-friendly Version

Interactive Discussion



Abstract

The interaction between marine boundary layer cellular cloudiness and surface fluxes of sensible and latent heat is investigated. The investigation focuses on the non-precipitating closed-cell state and the precipitating open-cell state at low geostrophic wind speed. The Advanced Research WRF model is used to conduct cloud-system-resolving simulations with interactive surface fluxes of sensible heat, latent heat, and of sea salt aerosol, and with a detailed representation of the interaction between aerosol particles and clouds. The mechanisms responsible for the temporal evolution and spatial distribution of the surface heat fluxes in the closed- and open-cell state are investigated and explained. It is found that the closed-cell state imposes its horizontal spatial structure on surface air temperature and water vapor, and, to a lesser degree, on the surface sensible and latent heat flux. The responsible mechanism is the entrainment of dry free tropospheric air into the boundary layer. The open-cell state drives oscillations in surface air temperature, water vapor, and in the surface fluxes of sensible heat, latent heat, and of sea salt aerosol. Here, the responsible mechanism is the periodic formation of clouds, rain, and of cold and moist pools with elevated wind speed. Open-cell cloud formation, cloud optical depth and liquid water path, and cloud and rain water path are identified as good predictors of the spatial structure of surface air temperature and sensible heat flux, but not of surface water vapor and latent heat flux. It is shown that the open-cell state creates conditions conducive to its maintenance by enhancing the surface sensible heat flux. The open-cell state also enhances the sea-salt flux relative to the closed-cell state. While the open-cell state under consideration is not depleted in aerosol and is insensitive to variations in sea-salt fluxes, in aerosol-depleted conditions, the enhancement of the sea-salt flux may replenish the aerosol needed for cloud formation and hence contribute to the maintenance of the open-cell state. Spatial homogenization of the surface fluxes is found to have only a small effect on cloud properties in the investigated cases. This indicates that sub-grid scale spatial variability in the surface flux of sensible and latent heat and of sea salt aerosol may not

Marine cellular cloudiness and surface heat fluxes

J. Kazil et al.

Title Page

Abstract

Introduction

Conclusions

References

Tables

Figures



Back

Close

Full Screen / Esc

Printer-friendly Version

Interactive Discussion



be required in large scale and global models to describe marine boundary layer cellular cloudiness.

1 Introduction

Stratocumulus clouds over the oceans play an important role for Earth's climate owing to their large areal coverage and the high contrast in albedo between the bright clouds and the dark sea underneath (Wood, 2012). Regular patterns in horizontal cloud structure, such as bands and several types of cells, first identified in satellite images (Krueger and Fritz, 1961; Agee, 1984) reflect different states of boundary layer dynamics (Atkinson and Zhang, 1996). This work focuses on two of these states, the closed-cell state and the precipitating open-cell state. The closed-cell state exhibits little or no surface rain and a cloud fraction close to unity. Its dynamics is stationary in character (Koren and Feingold, 2013), and driven by cloud-top radiative cooling that produces narrow downdrafts surrounding broader updrafts (Shao and Randall, 1996). This circulation pattern creates high optical depths in broad cell centers and reduced optical depths in the narrow periphery. In contrast, the precipitating open-cell state exhibits a low cloud fraction in broad, optically thin cell centers, surrounded by narrow rings of optically thick and sometimes heavily drizzling clouds (Stevens et al., 2005; Van Zanten and Stevens, 2005; Sharon et al., 2006). The dynamics is non-stationary and periodic in character, with oscillations driven by the formation of negative buoyancy in updrafts forming at convergence zones of three adjacent open cells (Feingold et al., 2010). Evaporation of rain below cloud base, which cools and eventually reverses the updrafts (Xue et al., 2008; Wang and Feingold, 2009a), has been identified as a key forcing of the open-cell state (Savic-Jovcic and Stevens, 2008). The resulting downdrafts lead to the formation of cold and moist pools at the surface, as well as to surface wind divergence (Jensen et al., 2000; Comstock et al., 2005; Stevens et al., 2005; Comstock et al., 2007; Wood et al., 2011).

Marine cellular cloudiness and surface heat fluxes

J. Kazil et al.

Title Page

Abstract

Introduction

Conclusions

References

Tables

Figures



Back

Close

Full Screen / Esc

Printer-friendly Version

Interactive Discussion



Marine cellular cloudiness and surface heat fluxes

J. Kazil et al.

Title Page

Abstract

Introduction

Conclusions

References

Tables

Figures

◀

▶

◀

▶

Back

Close

Full Screen / Esc

Printer-friendly Version

Interactive Discussion



The closed- and the open-cell state derive their relevance to the climate system from the difference in their cloud fraction and cloud radiative forcing, and from potential transitions between the two states. Rain at cloud base is thought to be a necessary (Stevens et al., 2005) but not a sufficient (Wood et al., 2011) condition for the transition from closed to open cells. However, even very weak rain (few tenths of mm d^{-1}) reaching the surface can initiate open-cell formation (Wang and Feingold, 2009a). Observations indicate that the reverse transition, from open- to closed-cells, also occurs in nature, and requires suppression of rain by enhanced aerosol concentrations such as from ship emissions (Goren and Rosenfeld, 2012), although simulations have not yet reproduced this phenomenon (Wang and Feingold, 2009b), hinting at the importance of environmental controls.

A multitude of mechanisms can lead to the development of rain in closed cells, and hence to open-cell formation, including perturbations in boundary layer moisture, temperature, aerosol concentration, and surface sensible and latent heat fluxes (Wang et al., 2010). Wang et al. (2010) found that large increases in surface sensible heat flux and/or latent heat flux are effective in triggering rain and the formation of open cells. Deepening of the boundary layer can also initiate rain formation and thus the transition from closed to open cells (Mechem et al., 2012). The causative effect of an increased surface sensible heat flux and of boundary layer deepening on the formation of rain and open cells is the basis of a proposed mechanism for the breaking of marine stratocumuli to trade wind cumuli (Rosenfeld et al., 2006): as the stratocumulus decks along the western coasts of continents are advected by the geostrophic flow towards the equator, hence towards warmer water and reduced subsidence, the associated increase in surface sensible heat flux and deepening of the boundary layer would result in the formation of rain, open cells, and eventually of trade wind cumuli. The prevailing mechanism for the evolution from stratocumulus to trade wind cumulus is thought to be decoupling, which occurs when the stratocumulus deck is advected over warmer water, resulting in a higher surface sensible heat flux, a deepening of the boundary layer, increased entrainment of free tropospheric air, and a higher surface latent heat flux,

with or without rain (Krueger et al., 1995; de Roode and Duijnkerke, 1997; Bretherton and Wyant, 1997).

In this work, the interaction between the closed- and open-cell state with the surface fluxes of sensible and latent heat is investigated. The investigation is motivated by the presence of cold and moist pools with surface wind divergence in the open-cell state, which have the potential to modify the surface flux of sensible and latent heat and of sea salt aerosol, relative to the closed-cell state. Such a modification could represent a feedback loop in the open-cell state, via the effects of surface heat and sea salt aerosol fluxes on cloud processes. The text is organized as follows: Sect. 2 gives a brief overview of the model used in the investigation. The simulations are described in Sect. 3, followed by a discussion of the results in Sect. 4. Conclusions are given in Sect. 5. Conventions used throughout this work include the definition of liquid water path as the vertically integrated mass of cloud and rain water; cloud fraction is the fractional area with a liquid water path $> 10 \text{ gm}^{-2}$.

2 Model

The Advanced Research WRF (ARW) model (Skamarock et al., 2008), with chemical and aerosol processes (WRF/Chem, Grell et al., 2005), and the modifications described in Kazil et al. (2011), is used. For the purpose of this work, all chemical and most aerosol processes are disabled in the model, with the exception of sea salt aerosol emissions (Clarke et al., 2006), aerosol water uptake (Petters and Kreidenweis, 2007), activation of aerosol to cloud droplets, cloud processing of aerosol via collision-coalescence, and aerosol dry and wet deposition. Perpetual night is assumed by disabling short-wave radiation, in order to isolate the processes under investigation from variability introduced by the diurnal cycle. Long-wave radiation is described with the Community Atmosphere Model scheme (CAM 3.0, Collins et al., 2004). The sub-grid scale eddy viscosity and diffusivity are calculated with the turbulence kinetic energy scheme of Deardorff (1972) to represent unresolved turbulence.

The ARW model calculates surface sensible (H_S) and latent (H_L) heat fluxes interactively from surface quantities. H_S and H_L are proportional to the horizontal wind speed $|\mathbf{U} + \mathbf{V}|$ at the lowest model level ($l = 1$), and to the surface-air temperature and humidity difference, respectively:

$$\begin{aligned} H_S &\propto (T_{\text{sea surface}} - T_{l=1})|\mathbf{U} + \mathbf{V}|_{l=1}, \\ H_L &\propto (Q_{\text{sea surface}} - Q_{l=1})|\mathbf{U} + \mathbf{V}|_{l=1}. \end{aligned} \quad (1)$$

\mathbf{U} and \mathbf{V} are the component vectors of the horizontal wind speed in the west–east and south–north directions, respectively. The proportionality coefficients are calculated using similarity theory (Skamarock et al., 2008, 8.3.1). $T_{l=1}$ and $Q_{l=1}$ are the air temperature and water vapor mixing ratio of air at the lowest model level, and will be referred to as surface air temperature and surface water vapor, respectively, throughout this work. $T_{\text{sea surface}}$ is the sea surface temperature, $Q_{\text{sea surface}}$ is the saturation water vapor mixing ratio of air at this temperature. The 10 m horizontal surface wind speed $|\mathbf{U} + \mathbf{V}|_{10\text{m}}$ is used in the calculation of the sea salt aerosol flux (Clarke et al., 2006).

The components U and V of the horizontal wind speed are decomposed into a geostrophic and a residual part in this work:

$$\begin{aligned} U &= u + u', \\ V &= v + v'. \end{aligned} \quad (2)$$

ARW was modified so that its Eulerian mass-coordinate dynamical core only operates on the residual wind field (u', v', w'), with the vertical wind speed w' . The surface flux of horizontal momentum due to surface drag is calculated from $U_{l=1}$ and $V_{l=1}$, which creates shear in the vertical profiles of u' and v' . u' and v' are nudged with Rayleigh damping towards 0 at the top of the model domain over a 250 m layer. Applying the ARW dynamical core to the residual wind field in this manner is akin to moving the model domain with the geostrophic wind, although its geographic location remains fixed. This approach facilitates the analysis of horizontal spatial structures such as closed and

Marine cellular cloudiness and surface heat fluxes

J. Kazil et al.

Title Page

Abstract

Introduction

Conclusions

References

Tables

Figures

◀

▶

◀

▶

Back

Close

Full Screen / Esc

Printer-friendly Version

Interactive Discussion



open cells, which remain stationary with respect to the domain. In the original implementation of ARW, the closed and open cells would be advected through the domain by the geostrophic wind.

3 Simulations

5 Simulations are conducted on a domain that is sufficiently large to allow statistical analysis of mesoscale organization, yet with a spatial and temporal resolution that enables the representation of individual cloud elements (cloud-system-resolving simulations, Randall et al., 2003). The domain covers an area of $100\text{ km} \times 100\text{ km}$ with a height of 1800 m. The horizontal (vertical) resolution is 300 m (30 m), respectively, the temporal resolution is 3 s. Periodic lateral boundary conditions are used. The setup has
10 been successfully used to simulate the transition from the closed- to the open-cell state (Wang and Feingold, 2009a,b; Wang et al., 2010; Kazil et al., 2011), and has been shown to capture the essence of finer resolution simulations (Wang and Feingold, 2009a). The domain is located at 122° W , 31.5° N , with a Coriolis parameter of
15 $7.62 \times 10^{-5}\text{ s}^{-1}$. A large scale divergence of $3.75 \times 10^{-6}\text{ s}^{-1}$ is assumed, which gives the large-scale subsidence at each level when multiplied by the altitude. The simulations are initialized on 11 July 2001 at 04:00:00 UT with idealized vertical profiles (Fig. 1) of potential temperature and total water (as water vapor mixing ratio). In the boundary layer, potential temperature is initialized with 288.3 K, and total water with 9.45 g kg^{-1} .
20 Small vertical and horizontal random variations are superposed on these initial profiles to set the boundary layer circulation in motion, for which a spin-up period of 3 h is allotted. Collision-coalescence, sea salt emissions, and aerosol dry deposition are disabled for the duration of the spin-up period. The sea surface temperature is held constant at 292.5 K, and a northwesterly geostrophic wind of $u = 1\text{ ms}^{-1}$ and $v = -1\text{ ms}^{-1}$ is prescribed. An inert tracer is used to diagnose entrainment of free tropospheric air into the
25 boundary layer. The inert tracer is initialized with the (arbitrary) number mixing ratio of 1 ppt above the inversion and with 0 ppt below. The idealized initial and boundary con-

Marine cellular cloudiness and surface heat fluxes

J. Kazil et al.

Title Page

Abstract

Introduction

Conclusions

References

Tables

Figures

◀

▶

◀

▶

Back

Close

Full Screen / Esc

Printer-friendly Version

Interactive Discussion



cloud water, and to lower optical depths. The open cells maintain their size over the 24 h that follow (Fig. 2d), but their walls become broken and less well-defined. The optical depth in many cell centers is now reduced to values < 0.5 (Fig. 2d).

Figure 3 shows time series of selected quantities in simulation S_c and S_o . Cloud fraction remains near unity in the closed-cell state of S_c , but declines continuously in the open-cell state of S_o (Fig. 3a), in accord with the progression in open-cell structure from 12 to 36 h seen in Fig. 2 (break-up of cell walls, reduced optical depth in the cell centers). Liquid water path (Fig. 3b) drops rapidly in both simulations once collision-coalescence has been enabled (at 3 h into the simulations), as the ensuing rain transports liquid water from the cloud into the sub-cloud layer. There, most of the rain evaporates, as is evident from the absence of surface rain in S_c , and from the very low surface rain early in S_o (Fig. 3c). The initial decline in liquid water path is steeper in S_o compared to S_c because of its lower initial aerosol concentration (Table 1), which accelerates collision-coalescence and rain formation. After the initial reduction, the liquid water path exhibits a periodic variation in S_o (Fig. 3b). A similar oscillation, with a later onset, emerges in the surface rain time series of S_o (Fig. 3c). The oscillations in open-cell surface rain were first described by Feingold et al. (2010), and shown to be a consequence of the spatial organization and rearrangement of the synchronized open-cell state.

The surface sensible and latent heat fluxes in simulation S_c and S_o are examined in Fig. 3d, e. The open-cell (S_o) sensible heat flux undergoes an initial boost followed by a slow gradual lapse (Fig. 3d); the closed-cell (S_c) sensible heat flux experiences an initial, more rapid reduction before settling into an asymptotic decline. The open-cell sensible heat flux exceeds its closed-cell counterpart by approximately a factor of 3 for most of the duration of the simulations. The open-cell latent heat flux jumps briefly at the outset, and then undergoes a nearly linear decline thereafter, while the closed-cell state latent heat flux remains nearly constant (Fig. 3e).

The open-cell surface heat fluxes exhibit oscillations reminiscent of those in liquid water path (Fig. 3b), as does the open-cell surface sea salt flux (Fig. 3f). The open-cell

Marine cellular cloudiness and surface heat fluxes

J. Kazil et al.

Title Page

Abstract

Introduction

Conclusions

References

Tables

Figures



Back

Close

Full Screen / Esc

Printer-friendly Version

Interactive Discussion



sea salt aerosol flux from the surface is also strongly enhanced (by up to a factor of 8) relative to the closed-cell state (Fig. 3f). This enhancement is transient, and the sea salt flux assumes almost identical values at the end of the simulations (after 36 h). Sea salt emissions are parameterized in the simulations as a function of the surface wind speed only, and the sea salt flux enhancement and oscillations reflect variations in the open-cell surface wind speed.

Figure 4 examines the causes for the temporal evolution of the surface heat fluxes in simulation \mathcal{S}_c and \mathcal{S}_o . The analysis is based on Eq. (1). In \mathcal{S}_c , the temporal evolution of the surface sensible heat flux is driven by air temperature rather than by surface wind speed – the surface layer warms over the course of the simulation, leading to a decrease in sensible heat flux which is not compensated by the concurrent increase in surface total horizontal wind speed (Fig. 4a). The limited influence of surface wind speed is confirmed by the absence of its hour-scale variability the sensible heat flux time series. In contrast, the hour-scale surface wind speed variability appears in the surface latent heat flux (Fig. 4b). This underscores the role of surface wind speed for latent heat flux in the closed-cell state, which contributes to its increase over the course of \mathcal{S}_c .

In the open-cell state (\mathcal{S}_o), surface total horizontal wind speed and surface air temperature act conjointly on the simulation time scale in enhancing or suppressing the surface sensible heat flux (Fig. 4c): Temperature is reduced when wind speed is enhanced and vice versa, resulting in a corresponding increase or decrease of sensible heat flux, respectively. This behavior also appears on shorter (hourly) time scales: the temporal anomaly of the wind speed, temperature, and sensible heat flux time series (Fig. 4e) reveals a tightly correlated, periodic behavior of these quantities in which wind speed and temperature act in accord to increase or decrease the sensible heat flux. The unlagged periodicity of the time series indicates an underlying mechanism that drives both surface wind speed and air temperature and thereby the surface sensible heat flux.

Marine cellular cloudiness and surface heat fluxes

J. Kazil et al.

Title Page

Abstract

Introduction

Conclusions

References

Tables

Figures

⏪

⏩

◀

▶

Back

Close

Full Screen / Esc

Printer-friendly Version

Interactive Discussion



Marine cellular cloudiness and surface heat fluxes

J. Kazil et al.

Title Page

Abstract

Introduction

Conclusions

References

Tables

Figures

◀

▶

◀

▶

Back

Close

Full Screen / Esc

Printer-friendly Version

Interactive Discussion



The surface latent heat flux in S_o declines on the simulation time scale by conjoint action of surface wind speed and water vapor (Fig. 4d): the temporal evolution of the wind speed is characterized by a general decline over the duration of the simulation, while water vapor has the opposite trend. On shorter (hourly) time scales (Fig. 4f), the tightly correlated periodic behavior, seen in the sensible heat flux (Fig. 4e), reappears. However, unlike in the case of sensible heat flux, where wind speed and temperature oscillations act in unison, the determinant quantities of latent heat flux, wind speed and water vapor, oscillate in discord – peaks in wind speed, which enhance the latent heat flux, coincide with peaks in water vapor, which suppress the latent heat flux. The unlagged periodicity of the time series indicates an underlying mechanism that drives both surface wind speed and water vapor and thereby the surface latent heat flux. The mechanism responsible for the oscillations in the surface sensible and latent heat flux and in the sea salt flux, as well as in their determinant quantities will be the focus of the next section.

Figure 5 shows the inversion height time series in simulation S_o and S_o . The inversion heights diverge early in the simulations, at 1060 m, after which the closed-cell state boundary layer (S_o) grows on average by 1.8 mm s^{-1} , while its open-cell counterpart (S_o) recedes on average by 1.65 mm s^{-1} . This means that free tropospheric air entrains into the boundary layer in the closed-cell state, while boundary layer air detrains into the free troposphere in the open-cell state.

4.2 Imprint of open-cell oscillations on boundary layer base properties

The tightly correlated oscillations in the open-cell (S_o) surface heat fluxes and their determinant quantities surface wind speed, temperature, and water vapor (Fig. 4c–f) indicate a common underlying mechanism. It will be shown that this mechanism is the synchronization of the open-cell state (Feingold et al., 2010), in which the periodic formation of updrafts, which occurs when surface outflows from a preceding open cell generation converge, leads to the formation of clouds, rain, downdrafts, cold and moist pools, and surface wind divergence. These drive surface air temperature and water

vapor, and eventually surface heat fluxes. Domain-wide oscillations of dynamics, cloud properties, and surface rain will be identified, and their causal relationship to the oscillations in surface wind speed, surface air temperature and water vapor, and ultimately to the surface heat fluxes demonstrated.

5 Figure 6 shows the time series of latent heat release (heating of the air from condensation of water vapor), liquid water path, and surface rain, and their temporal anomalies in simulation \mathcal{S}_0 . Latent heat release is used to diagnose cloud-forming dynamics: as water vapor condenses in updrafts, latent heat is released. A peak in the latent heat release time series indicates simultaneous cloud-forming updrafts in the domain.
10 The three time series exhibit oscillations with a mean period of ≈ 2 h (Fig. 6a). This is the open-cell re-arrangement period, during which one generation of open cells spawns the next (Feingold et al., 2010). The temporal anomalies of the time series (Fig. 6b) reveal delays which reflect their causal relationships: latent heat release, indicating cloud-forming updrafts, leads the oscillations, followed by liquid water path, which builds up in the updrafts. The growing liquid water path renders rain formation by collision-coalescence more efficient. Some of the resulting rain arrives, with a delay, at the surface. The persistence of the oscillations and of their delay pattern demonstrates the domain-wide synchronization of the open-cell dynamics over the duration of simulation \mathcal{S}_0 .

20 Figure 7 shows the temporal anomaly of surface rain, plotted with the anomaly of surface air temperature, water vapor, and total horizontal wind speed. The time series exhibit a periodic pattern which constitutes an extension of the oscillations seen in Fig. 6. Here, surface rain peaks are followed by dips in surface air temperature, hikes in surface water vapor, and increases in surface wind speed. The causality of this sequence can be explained with downdrafts, which, cooled by evaporation of rain water, form surface cold pools, associated with surface wind divergence (Jensen et al., 2000; Comstock et al., 2005, 2007; Stevens et al., 2005; Wood et al., 2011). The applicability of this paradigm will be demonstrated by analysis of the spatial distribution of the quantities involved.
25

**Marine cellular
cloudiness and
surface heat fluxes**

J. Kazil et al.

Title Page

Abstract

Introduction

Conclusions

References

Tables

Figures

◀

▶

◀

▶

Back

Close

Full Screen / Esc

Printer-friendly Version

Interactive Discussion



filtering), respectively: surface air temperature is low and water vapor high at locations of high residual horizontal surface wind speed. Visual inspection of Fig. 8a confirms that the residual wind speed diverges and is highest around rain locations. Precipitating downdrafts hence depress surface air temperature and raise surface water vapor, and form cold pools with elevated humidity, despite the low correlation of surface air temperature and surface water vapor. We hypothesise that the radial distribution of surface air temperature and water vapor in the cold pools and its extension around the cold pools (Fig. 9c, d) is responsible for the fact that surface air temperature correlates better than surface water vapor with surface rain: temperature is lowest in the center of the cold pools, increases with distance from their centers, and is highest outside the cold pools (Fig. 9c). In contrast, water vapor is generally not, as one might expect, highest in the cold pool centers, where surface rain is strongest, but in water vapor “halos” along their periphery, where the cold pool outflows are strongest (see, e.g., the cold pool located at 88 km west–east and 32 km south–north in Fig. 9d). Outside cold pools, water vapor is depressed. It can be argued that the radial variation of surface air temperature and water vapor inside the cold pools is due to the action of the surface sensible and latent heat fluxes (Fig. 9e, f), which, driven by the divergent surface wind field in the cold pools, heat and humidify the air. Consequently, the air that has traveled farthest from the cold pool centers would be warmest and most humid.

4.3 Imprint of spatial organization on boundary layer base properties

The imprint of the closed- and open-cell state dynamical and cloud structure on the spatial distribution of boundary layer base properties is discussed here. The spatial structure of the closed-cell state will be shown to determine the surface distribution of surface air temperature and water vapor by entrainment of dry free tropospheric air, and, to a lesser degree, the surface sensible and latent heat fluxes. Open-cell cloud formation, optical depth, and cloud water path, followed by rain water path will be established as predictors of the spatial distribution of surface air temperature and surface sensible heat flux, but not of surface water vapor and of surface latent heat flux.

Marine cellular cloudiness and surface heat fluxes

J. Kazil et al.

Title Page

Abstract

Introduction

Conclusions

References

Tables

Figures



Back

Close

Full Screen / Esc

Printer-friendly Version

Interactive Discussion



4.3.1 Closed-cell state

Figure 10a shows cloud optical depth and the surface mixing ratio of an inert tracer in the closed-cell state at a given time in simulation \mathcal{S}_\bullet (see Fig. 2a for an unobstructed view of the cloud structure). The inert tracer mixing ratio was initialized with 1 ppt in the free troposphere and with zero in the boundary layer. As the inversion rises in \mathcal{S}_\bullet (Fig. 5), the inert tracer is entrained with free tropospheric air into the boundary layer. Visual inspection of Fig. 10a reveals elevated inert tracer surface mixing ratios at locations where cloud optical depth is low. Reduced optical depth is associated with downdrafts. Conversely, inert tracer surface mixing ratios are depressed at locations of high cloud optical depth, which are associated with updrafts. The spatial correlation coefficient of cloud optical depth and the inert tracer surface mixing ratio of -0.34 at the time in question (Fig. 10a), although not particularly high, reflects this association; the correlation coefficient improves to -0.51 after filtering (Supplement, Fig. A2a). The imprint of the closed-cell state dynamics on the boundary layer base is also illustrated in Fig. 10b, which shows the surface distribution of the inert tracer together with the residual horizontal surface wind field. The inert tracer is more abundant at locations of surface divergence, which, owing to mass continuity, are locations of downdrafts. The association of inert tracer concentration and surface divergence is brought out clearly by applying a spatial filter (Supplement, Fig. A2b).

The surface distribution of the inert tracer is highly correlated with the distribution of surface air temperature ($r = 0.93$, Fig. 10c) and water vapor mixing ratio ($r = -0.94$, Fig. 10d): surface air temperature is enhanced (depressed) and water vapor depressed (enhanced) at locations of high (low) inert tracer mixing ratios, respectively. The high correlations are expected in the closed-cell state, in which entrainment of dry free tropospheric air, by reducing the water content of descending air parcels and thereby latent heat uptake by evaporation during their descent, leads to drier and warmer air at the surface. This is the mechanism by which the horizontal spatial structure of the closed-cell state imprints itself onto surface air temperature and water vapor.

[Title Page](#)[Abstract](#)[Introduction](#)[Conclusions](#)[References](#)[Tables](#)[Figures](#)[◀](#)[▶](#)[◀](#)[▶](#)[Back](#)[Close](#)[Full Screen / Esc](#)[Printer-friendly Version](#)[Interactive Discussion](#)

Marine cellular cloudiness and surface heat fluxes

J. Kazil et al.

Title Page

Abstract

Introduction

Conclusions

References

Tables

Figures



Back

Close

Full Screen / Esc

Printer-friendly Version

Interactive Discussion



The spatial structure of the closed-cell state also emerges in the surface heat fluxes, as they respond to surface air temperature and water vapor (Eq. 1). The surface sensible heat flux is reduced at locations with higher inert tracer levels (Fig. 10e), where downdrafts supply warmer and drier air. Conversely, the latent heat flux is enhanced at these downdraft locations (Fig. 10f). Spatial filtering renders the connection clearly apparent (Supplement, Fig. A2e, f). The correlation coefficients of the surface sensible and latent heat flux with the inert tracer are, however, only $r = -0.45$ (Fig. 10e) and $r = -0.6$ (Fig. 10f), respectively, lower than the correlation coefficients between the inert tracer and surface air temperature ($r = 0.93$, Fig. 10c) and water vapor ($r = -0.94$, Fig. 10d). In other words, entrainment of dry free tropospheric air determines surface air temperature and water vapor to a greater degree than it determines surface heat fluxes. This is because the surface heat fluxes not only vary with surface air temperature and water vapor, but also with the total surface wind speed (Eq. 1): the total surface wind speed correlates well with the sensible and latent heat flux at $r = 0.73$ and $r = 0.82$, respectively, in simulation \mathcal{S}_o (for the time shown in Fig. 10). In conclusion, the closed-cell circulation imposes its horizontal spatial structure on boundary layer base properties such as surface air temperature and water vapor by entrainment of dry free tropospheric air, and, to a lesser degree, on the surface sensible and latent heat fluxes.

4.3.2 Open-cell state

Lagged spatial correlations between quantities in the open-cell state (\mathcal{S}_o) are analyzed in this section. An extremum in the lagged spatial correlation coefficient is interpreted as the manifestation of a causal relationship in which the spatial distribution of one quantity determines the spatial distribution of the other, after a delay or lag. The focus is on the open-cell state (\mathcal{S}_o), whose cellular structure changes approximately every two hours, and where such lags materialize. In the more stationary (Feingold et al., 2010; Koren and Feingold, 2013) closed-cell state (\mathcal{S}_c), spatial correlations between quantities vary slowly with lag time, and peaks occur at a zero lag. Visual examples of lagged

spatial correlations in simulation S_o are given in Fig. 11 (Supplement, Fig. A3, after filtering). Tables 2 and 3 provide spatial correlation coefficients of selected quantities at lags of 0–60 min, for two times in S_o .

To facilitate the subsequent discussion, the role of open-cell dynamics for surface air temperature, water vapor, and surface heat fluxes in the open-cell state is revisited. The residual wind speed correlates better (Table 2a) with surface air temperature and water vapor than the total wind speed (Table 2b). This underscores the role of the open-cell circulation in determining the spatial distribution of surface quantities. The underlying mechanism is the formation of moist cold pools and of surface divergence by precipitating downdrafts (Sect. 4.2). A consequence is a good correlation of the residual wind speed with the surface sensible heat flux, although not with the latent heat flux (Table 2a). The different behavior of surface sensible and latent heat flux arises from the synergetic action of increased surface wind speed and reduced temperature in the cold pools in driving the surface sensible heat flux, while the elevated surface wind speed and enhanced water vapor in the cold pools counteract each other in driving the surface latent heat flux (Sect. 4.1). Hence the residual open-cell circulation drives surface air temperature, water vapor, the surface sensible heat flux, but to a lesser degree the surface latent heat flux. In the following it will be shown that cloud formation, cloud optical depth and liquid water path, and cloud and rain water path are good predictors of the spatial distribution of surface air temperature and sensible heat flux in the open-cell state, but not of surface water vapor and surface latent heat flux.

The spatial distribution in latent heat release path (vertical integral), which diagnoses cloud-forming updrafts, and the lagged spatial distribution of surface air temperature and sensible heat flux is shown in Fig. 11a, b, respectively (Supplement, Fig. A3a, b after filtering). Latent heat release occurs at locations of future cold pools and areas of elevated sensible heat flux. The corresponding spatial correlation coefficients reach their extrema at a lag of ≈ 40 min (Table 3a). Cloud formation hence predicts surface air temperature and sensible heat flux. Cloud formation is, however, not a good predictor of surface water vapor and surface latent heat flux, with comparably low lagged correlation

Marine cellular cloudiness and surface heat fluxes

J. Kazil et al.

Title Page

Abstract

Introduction

Conclusions

References

Tables

Figures

◀

▶

◀

▶

Back

Close

Full Screen / Esc

Printer-friendly Version

Interactive Discussion



coefficients (Table 3a). We propose that this is due to the aforementioned discordant action of surface wind speed and enhanced water vapor in driving the cold pool surface latent heat flux (Sect. 4.1), and the formation of cold pool water vapor halos (Sect. 4.2).

Figure 11 shows the spatial distribution of cloud optical depth with the lagged spatial distribution of surface air temperature (c) and surface sensible heat flux (d), respectively. The corresponding spatial correlation coefficients reach extrema at a lag of 20–30 min (Table 3b). Cloud optical depth hence becomes a predictor of surface air temperature and surface sensible heat flux approximately 10 min after cloud formation. Liquid water path is a similarly good predictor of the spatial distribution of surface air temperature and surface sensible heat flux (Table 3c), with a lag close to that of cloud optical depth (Table 3b).

The lagged spatial correlation of cloud water path and rain water path, the two constituents of liquid water path, with surface temperature and sensible heat flux illustrates a noteworthy manifestation of cloud microphysics: the lag at which the correlation of cloud water path with surface air temperature and surface sensible heat flux becomes extremal is ≈ 30 min (Table 3d). The lag is shorter, with ≈ 20 min, for the rain water path (Table 3e). Hence cloud water predicts the distribution of surface air temperature and surface sensible heat flux with a greater lead time than rain water – this is because rain water first needs to form from cloud water by collision-coalescence. The spatial structure of rain water path, and the lagged spatial structure of surface air temperature and surface sensible heat flux is shown in Fig. 11e, f (Supplement, Fig. A3e, f after filtering), with the open-cell structure clearly visible.

In summary, based on lagged spatial correlation analysis, cloud formation, cloud optical depth and liquid water path, and cloud and rain water path are good predictors of the spatial distribution of surface air temperature and sensible heat flux in the open-cell state, but not of surface water vapor and surface latent heat flux. As a consequence of the causal chain of latent heat release in cloud-forming updrafts, the associated buildup of liquid water path and cloud optical depth, formation of cloud droplets and subsequently of rain droplets, these quantities predict surface air temperature and sensible

Marine cellular cloudiness and surface heat fluxes

J. Kazil et al.

Title Page

Abstract

Introduction

Conclusions

References

Tables

Figures

◀

▶

◀

▶

Back

Close

Full Screen / Esc

Printer-friendly Version

Interactive Discussion



heat flux with lead times decreasing from ≈ 40 min to ≈ 20 min. These lead times are subject to some uncertainty, owing to the temporal resolution of 10 min at which the simulation data were sampled.

4.4 Maintenance of the open-cell state

It will be demonstrated that the open-cell state in simulation S_o creates surface heat fluxes, specifically a surface sensible heat flux, by which it is maintained. To this end, simulation S_{\otimes} was conducted, which has a setup that is identical to the open-cell simulation S_o , except that S_{\otimes} is forced with spatially homogenized surface fluxes of sensible heat, latent heat, and sea salt from the closed-cell simulation S_c . The cloud structure in simulation S_{\otimes} is shown in Fig. 12; Fig. 13 compares time series of selected quantities in simulation S_{\otimes} and S_o . Simulation S_{\otimes} develops an open-cell state which is present after 12 h (Fig. 12a). This open-cell state does not endure; after 36 h (Fig. 12b) it has been replaced by a state that exhibits numerous localized cloud features, reminiscent of a field of shallow cumuli. Cloud fraction (Fig. 13a) is slightly higher, and liquid water path (Fig. 13b) and surface rain (Fig. 13c) are notably enhanced in simulation S_{\otimes} relative to S_o . Hence when used to drive the open-cell state, the closed-cell state surface fluxes promote rain formation and surface rain, and are unable to maintain the open-cell state. This raises the question as to which of the open-cell surface fluxes from simulation S_o – sensible heat, latent heat, or sea salt – is required or sufficient for the perpetuation of the open-cell state. The enhanced sensible heat flux in S_o (Fig. 13d) may warm updrafts, or the enhanced sea salt flux (Fig. 13f) could supply condensation nuclei for cloud formation – either of which may prevent the buildup of liquid water path and the increase in surface rain seen in simulation S_{\otimes} (Fig. 13b, c). To elucidate this matter, simulations S'_o and S''_o were conducted (Table 1).

The setup of simulation S'_o differs from that of S_o in that sea salt emissions are disabled. S'_o produces an open-cell state much like S_o , with nearly indistinguishable time series of cloud fraction, cloud optical depth, liquid water path, and surface rain (Supplement, Sect. B). Hence the initial aerosol concentration in S_o is not depleted by surface

Marine cellular cloudiness and surface heat fluxes

J. Kazil et al.

Title Page

Abstract

Introduction

Conclusions

References

Tables

Figures

◀

▶

◀

▶

Back

Close

Full Screen / Esc

Printer-friendly Version

Interactive Discussion



rain to a level at which sea salt emissions would be requisite to supply condensation nuclei, and the sea salt flux enhancement in \mathcal{S}_o relative to \mathcal{S}_c is not required to maintain the open-cell state. The argument is complemented by the fact that in \mathcal{S}_{\otimes} , despite higher surface rain, the total aerosol concentration is higher than in \mathcal{S}_o (Fig. 13c, j).

5 The setup of simulation \mathcal{S}_o'' differs from that of \mathcal{S}_o in that the spatially homogenized surface latent and sea salt flux from the closed-cell simulation \mathcal{S}_c , and the spatially homogenized surface sensible heat flux from the open-cell simulation \mathcal{S}_o are used. The open-cell state is maintained in \mathcal{S}_o'' , and time series of cloud fraction, cloud optical depth, liquid water path and other quantities exhibit no appreciable difference to \mathcal{S}_o , with the exception of a mild enhancement of surface rain (Supplement, Sect. C). The open-cell surface sensible heat flux by itself is hence able to maintain the open-cell state of simulation \mathcal{S}_o .

This completes the task of showing that it is the surface sensible heat flux in simulation \mathcal{S}_o which maintains the open-cell state. However, several points surrounding this finding deserve attention and will be discussed in the following. Wang et al. (2010) determined that a source of aerosol, such as sea salt emissions is required to maintain the open-cell state, to compensate for aerosol removal by surface rain, and that without such a source, the boundary layer may collapse. This is not in contradiction to the above finding that in the simulation \mathcal{S}_o , sea salt emissions matter not; the reason is that in the present simulations, unlike those in Wang et al. (2010), surface rain does not deplete aerosol to a level at which a source would be required for its replenishment. Nonetheless, sea salt emissions are amplified by up to a factor of eight in the open-cell simulation \mathcal{S}_o compared to the closed-cell simulation \mathcal{S}_c (Fig. 5f). Although in the present simulations, this enhancement plays no role in the evolution of the open-cell state, and notwithstanding the transient nature of the enhancement, we conjecture that in conditions that are more depleted in aerosol, it could contribute to the replenishment of aerosol removed by surface rain. In other words, in such conditions, the open-cell state would create both a surface sensible heat and sea salt flux by which it is maintained.

Marine cellular cloudiness and surface heat fluxes

J. Kazil et al.

[Title Page](#)[Abstract](#)[Introduction](#)[Conclusions](#)[References](#)[Tables](#)[Figures](#)[Back](#)[Close](#)[Full Screen / Esc](#)[Printer-friendly Version](#)[Interactive Discussion](#)

**Marine cellular
cloudiness and
surface heat fluxes**

J. Kazil et al.

Title Page

Abstract

Introduction

Conclusions

References

Tables

Figures

◀

▶

◀

▶

Back

Close

Full Screen / Esc

Printer-friendly Version

Interactive Discussion



In what follows, the evolution of the simulation S_{\otimes} will be analyzed, and an explanation for the decay of its open-cell state will be given. Most insight is gained by examination of surface air temperature, surface water vapor, and the condensation level (Fig. 13g–i). Simulation S_{\otimes} has a cooler (Fig. 13g) and more humid (Fig. 13h) surface layer than S_{\circ} . This is a consequence of the lower sensible heat flux (Fig. 13d), likely in conjunction with more cooling and humidification below cloud base due to higher evaporation accompanying enhanced surface rain (Fig. 13c). The surface latent heat flux is lower in the initial 16 h of simulation S_{\otimes} compared to S_{\circ} , and therefore can not readily explain the more humid surface layer in S_{\otimes} . The cooler and more humid surface layer gives rise to cooler and more humid updrafts, wherein water vapor saturates at a lower altitude, illustrated by a lower condensation level (Fig. 13i). The result is an increased liquid water path (Fig. 13b) and a higher surface rain rate (Fig. 13c). It is central to the understanding of the decay of the open-cell state in simulation S_{\otimes} that this higher surface rain rate is accompanied by an increase in the number of rain regions, as will be shown next.

Figure 14 shows the spatial distribution of surface rain after 12 and 36 h in simulations S_{\circ} and S_{\otimes} . A numerical algorithm was used to identify contiguous regions larger than a given size ($\geq 1 \text{ km}^2$) with surface rain rates exceeding a given threshold ($\geq 1 \text{ mm d}^{-1}$). The number of rain locations increases in simulation S_{\otimes} compared to simulation S_{\circ} ; the increase is quantified in the form of a time series in Fig. 15. The increase in rain locations in simulation S_{\otimes} arises as open-cell walls, which form at convergence zones of two adjacent cells, produce surface rain in addition to the convergence zones of three adjacent cells (Feingold et al., 2010), owing to the cooler and more humid surface layer in S_{\otimes} . In contrast, surface rain in simulation S_{\circ} is largely limited to the convergence zones of three adjacent cells, which constitute future open-cell centers. The increased propensity of cell walls to precipitate causes the collapse of the open-cell state in simulation S_{\otimes} , as it spawns an ever-increasing number of potential future cell centers, while cell walls disappear. The growing number of rain locations also results in a de-synchronization of the system: the open-cell state in S_{\otimes} initially ex-

hibits domain-wide oscillations of cloud formation (diagnosed by the latent heat release path), liquid water path, and surface rain (Fig. 16), as in simulation \mathcal{S}_o (Fig. 6). However, in the final 6 h of \mathcal{S}_o , as the number of rain locations increases most dramatically, the amplitude of the oscillations fades away. This indicates that dynamics, cloud formation, and surface rain are not connected anymore in a synchronized cycle (Feingold et al., 2010), but proceed independently at the different locations of the domain.

To complete the discussion of the maintenance of the precipitating open-cell state, the open problem of its stability and the reasons for its relevance shall be briefly noted. Figure 3d–f shows that once they have peaked, the surface fluxes of sensible and latent heat as well as of sea salt aerosol in simulation \mathcal{S}_o continuously decrease. Even though it was shown that the open-cell state in simulation \mathcal{S}_o creates surface fluxes required for its perpetuation, this decrease with time raises the question whether, and in what conditions the open-cell state can attain a steady state, and thereby maintain itself indefinitely, or whether, and in what conditions, and how quickly the continuous decrease in the surface fluxes causes its downfall. Prima facie, this question may appear unimportant, because in nature, the open-cell state will be subject to changing environmental conditions and a steady state may never materialize – e.g., the air mass in which the open-cell state is embedded may be advected along a gradient in sea surface temperature, which would change the surface sensible heat flux. However, it is the stability of the open-cell state or the absence thereof in given conditions which prevents or enables changes in the environmental conditions to extend or shorten the lifetime of the open-cell state. The question also has merit from a conceptual point of view, in the sense of understanding the extent to which precipitating open-cell cloudiness should be regarded as a potentially stable, or a purely transitional marine boundary layer state. These questions will be addressed in future work.

**Marine cellular
cloudiness and
surface heat fluxes**

J. Kazil et al.

Title Page

Abstract

Introduction

Conclusions

References

Tables

Figures

◀

▶

◀

▶

Back

Close

Full Screen / Esc

Printer-friendly Version

Interactive Discussion



4.5 The role of surface flux spatial inhomogeneity for the closed- and open-cell state

It is demonstrated that the spatial distribution of surface fluxes has little bearing on cloud properties in the considered closed- and the open-cell state. To this end, closed- and the open-cell simulations were conducted with spatially homogenized surface fluxes from the simulations \mathcal{S}_c and \mathcal{S}_o . These are the simulations \mathcal{S}_{c_0} and \mathcal{S}_{o_0} , respectively (Table 1). Figure 17 shows selected quantities from simulation \mathcal{S}_{c_0} and \mathcal{S}_{o_0} (closed-cell state), and Fig. 18 from simulation \mathcal{S}_c and \mathcal{S}_o (open-cell state). Spatial homogenization of the surface fluxes has no appreciable effect on cloud fraction, liquid water path, and surface rain. This finding indicates that sub-grid scale spatial variability in surface heat and sea salt fluxes is not required in large scale and global models to describe marine boundary layer cellular cloudiness. However, a greater sample of simulations to account for variability that exists in the cloudy marine boundary layer would be required for a generalization of this finding beyond the cases considered here.

4.6 Additional remarks

The marine boundary layer cellular cloud states considered in this work are specific to the conditions used in the simulations. In nature, the gamut of conditions, processes, and mechanisms not considered in this work, and the associated variability in cellular cloudiness may give rise to behavior not captured here. The lack of generality of the examples in this work does not diminish the insight into the workings of the cloudy marine boundary layer.

The comparably slow geostrophic wind speed of $\sqrt{2} \text{ m s}^{-1}$ used in this work results in only weak surface wind shear, and by consequence, limited shear-induced circulation. This not only leads to a comparably small distortion of the horizontal features in the dynamics and cloud structure, but also to little horizontal shift between features at the boundary layer top and at its base. These benefits of a slow geostrophic wind speed facilitate the spatial correlation analysis conducted here. At higher geostrophic wind

Marine cellular cloudiness and surface heat fluxes

J. Kazil et al.

Title Page

Abstract

Introduction

Conclusions

References

Tables

Figures

◀

▶

◀

▶

Back

Close

Full Screen / Esc

Printer-friendly Version

Interactive Discussion



speeds, horizontal distortion and shift of spatial features may render such an analysis more demanding or unfeasible, and possibly yield degraded spatial correlation coefficients, although the mechanisms identified in this work may still be in play. It should be noted that at geostrophic wind speeds greater than used in this work, the total wind speed should become increasingly more, and the residual circulation increasingly less important in driving the surface fluxes.

5 Conclusions

A set of idealized cloud-system-resolving simulations with the Advanced Research WRF model is presented to give insight into the interaction between marine boundary layer cellular cloudiness and surface fluxes of sensible heat, latent heat, and of sea salt aerosol. The mechanisms responsible for the temporal evolution and spatial distribution of the surface heat fluxes in the non-precipitating closed-cell state and the precipitating open-cell state are investigated and explained. It is found that the closed-cell state imposes its horizontal spatial structure on surface air temperature and water vapor, and, to a lesser degree, on the surface sensible and latent heat flux. The responsible mechanism is the entrainment of dry free tropospheric air into the boundary layer. The open-cell state drives oscillations in surface air temperature, water vapor, and in the surface fluxes of sensible heat, latent heat, and of sea salt aerosol. Here, the responsible mechanism is the periodic formation of clouds, rain, and of cold and moist pools with elevated wind speed. Open-cell cloud formation, cloud optical depth and liquid water path, and cloud and rain water path are identified as good predictors of the spatial structure of surface air temperature and sensible heat flux, but not of surface water vapor and latent heat flux. It is shown that the open-cell state creates conditions conducive to its maintenance by enhancing the surface sensible heat flux. The open-cell state also enhances the sea-salt flux relative to the closed-cell state. While the open-cell state under consideration is not depleted in aerosol and is insensitive to variations in sea-salt fluxes, in aerosol-depleted conditions, the enhancement

Marine cellular cloudiness and surface heat fluxes

J. Kazil et al.

Title Page

Abstract

Introduction

Conclusions

References

Tables

Figures

◀

▶

◀

▶

Back

Close

Full Screen / Esc

Printer-friendly Version

Interactive Discussion



Marine cellular cloudiness and surface heat fluxes

J. Kazil et al.

Title Page

Abstract

Introduction

Conclusions

References

Tables

Figures

◀

▶

◀

▶

Back

Close

Full Screen / Esc

Printer-friendly Version

Interactive Discussion



of the sea-salt flux may replenish the aerosol needed for cloud formation and hence contribute to the maintenance of the open-cell state. Furthermore, spatial homogenization of the surface fluxes is found to have only a small effect on cloud properties in the investigated cases. This indicates that sub-grid scale spatial variability in the surface flux of sensible and latent heat and of sea salt aerosol may not be required in large scale and global models to describe marine boundary layer cellular cloudiness.

Supplementary material related to this article is available online at:

[http://www.atmos-chem-phys-discuss.net/13/18855/2013/](http://www.atmos-chem-phys-discuss.net/13/18855/2013/acpd-13-18855-2013-supplement.pdf)

[acpd-13-18855-2013-supplement.pdf](http://www.atmos-chem-phys-discuss.net/13/18855/2013/acpd-13-18855-2013-supplement.pdf).

Acknowledgements. Jan Kazil and Graham Feingold are supported by the US Department of Energy (DOE) Atmospheric System Research Program grant DE-SC0006972. Takano Yu Yamaguchi is supported by the US National Oceanic and Atmospheric Administration (NOAA) Climate Program Office through the Climate Process Team, Cloud Macrophysical Parameterization and its Application to Aerosol Indirect Effects. Jan Kazil, Graham Feingold, and Takano Yu Yamaguchi are supported by NOAA's Climate Goal. Hailong Wang is supported by the DOE Office of Science Earth System Modeling Program. The Pacific Northwest National Laboratory (PNNL) is operated for DOE by Battelle Memorial Institute under contract DE-AC05-76RLO1830. Simulations were carried out on the NOAA Research & Development High Performance Computing System.

References

- Agee, E. M.: Observations from space and thermal convection: a historical perspective, *B. Am. Meteorol. Soc.*, 65, 938–949, doi:10.1175/1520-0477(1984)065<0938:OFSATC>2.0.CO;2, 1984. 18857
- Atkinson, B. W. and Zhang, J. W.: Mesoscale shallow convection in the atmosphere, *Rev. Geophys.*, 34, 403–431, doi:10.1029/96RG02623, 1996. 18857

Marine cellular cloudiness and surface heat fluxes

J. Kazil et al.

Title Page

Abstract

Introduction

Conclusions

References

Tables

Figures

◀

▶

◀

▶

Back

Close

Full Screen / Esc

Printer-friendly Version

Interactive Discussion



- Berner, A. H., Bretherton, C. S., and Wood, R.: Large-eddy simulation of mesoscale dynamics and entrainment around a pocket of open cells observed in VOCALS-REx RF06, *Atmos. Chem. Phys.*, 11, 10525–10540, doi:10.5194/acp-11-10525-2011, 2011. 18867
- Bretherton, C. S. and Wyant, M. C.: Moisture transport, lower-tropospheric stability, and decoupling of cloud-topped boundary layers, *J. Atmos. Sci.*, 54, 148–167, doi:10.1175/1520-0469(1997)054<0148:MTLTA>2.0.CO;2, 1997. 18859
- Clarke, A. D., Owens, S. R., and Zhou, J.: An ultrafine sea-salt flux from breaking waves: implications for cloud condensation nuclei in the remote marine atmosphere, *J. Geophys. Res.*, 111, D06202, doi:10.1029/2005JD006565, 2006. 18859, 18860
- Collins, W. D., Rasch, P. J., Boville, B. A., Hack, J. J., McCaa, J. R., Williamson, D. L., Kiehl, J. T., Briegleb, B., Blitz, C., Lin, S.-J., Zhang, M., and Dai, Y.: Description of the NCAR Community Atmosphere Model (CAM 3.0), Tech. Rep. NCAR/TN-464+STR, National Center for Atmospheric Research, Boulder, CO, USA, 2004. 18859
- Comstock, K. K., Bretherton, C. S., and Yuter, S. E.: Mesoscale variability and drizzle in Southeast Pacific stratocumulus, *J. Atmos. Sci.*, 62, 3792–3807, doi:10.1175/JAS3567.1, 2005. 18857, 18866
- Comstock, K. K., Yuter, S. E., Wood, R., and Bretherton, C. S.: The three-dimensional structure and kinematics of drizzling stratocumulus, *Mon. Weather Rev.*, 135, 3767–3784, doi:10.1175/2007MWR1944.1, 2007. 18857, 18866
- de Roode, S. R. and Duynkerke, P. G.: Observed Lagrangian transition of stratocumulus into cumulus during ASTEX: mean state and turbulence structure, *J. Atmos. Sci.*, 54, 2157–2173, doi:10.1175/1520-0469(1997)054<2157:OLTOSI>2.0.CO;2, 1997. 18859
- Deardorff, J. W.: Numerical investigation of neutral and unstable planetary boundary layers, *J. Atmos. Sci.*, 29, 91–115, doi:10.1175/1520-0469(1972)029<0091:NIONAU>2.0.CO;2, 1972. 18859
- Feingold, G., Koren, I., Wang, H., Xue, H., and Brewer, A. W.: Precipitation-generated oscillations in open cellular cloud fields, *Nature*, 466, 849–852, doi:10.1038/nature09314, 2010. 18857, 18863, 18865, 18866, 18870, 18875, 18876
- Goren, T. and Rosenfeld, D.: Satellite observations of ship emission induced transitions from broken to closed cell marine stratocumulus over large areas, *J. Geophys. Res.*, 117, D17206, doi:10.1029/2012JD017981, 2012. 18858

- Grell, G. A., Peckham, S. E., Schmitz, R., McKeen, S. A., Frost, G., Skamarock, W. C., and Eder, B.: Fully coupled “online” chemistry within WRF model, *Atmos. Environ.*, 39, 6957–6975, doi:10.1016/j.atmosenv.2005.04.027, 2005. 18859
- Jensen, J., Lee, S., Krummel, P. B., Katzfey, J., and Gogoasa, D.: Precipitation in marine cumulus and stratocumulus – Part 1: Thermodynamic and dynamic observations of closed cell circulations and cumulus bands, *Atmos. Res.*, 54, 117–155, doi:10.1016/S0169-8095(00)00040-5, 2000. 18857, 18866
- Kazil, J., Wang, H., Feingold, G., Clarke, A. D., Snider, J. R., and Bandy, A. R.: Modeling chemical and aerosol processes in the transition from closed to open cells during VOCALS-REx, *Atmos. Chem. Phys.*, 11, 7491–7514, doi:10.5194/acp-11-7491-2011, 2011. 18859, 18861
- Koren, I. and Feingold, G.: Adaptive behavior of marine cellular clouds, *Nature Sci. Rep.*, under review, 2013. 18857, 18870
- Krueger, A. F. and Fritz, S.: Cellular cloud patterns revealed by Tiros I, *Tellus*, 13, 1–7, doi:10.1111/j.2153-3490.1961.tb00061.x, 1961. 18857
- Krueger, S. K., McLean, G. T., and Fu, Q.: Numerical simulation of the stratus-to-cumulus transition in the subtropical marine boundary layer, Part 1: Boundary-layer structure, *J. Atmos. Sci.*, 52, 2839–2850, doi:10.1175/1520-0469(1995)052<2839:NSOTST>2.0.CO;2, 1995. 18859
- Mechem, D. B., Yuter, S. E., and de Szoeke, S. P.: Thermodynamic and aerosol controls in Southeast Pacific stratocumulus, *J. Atmos. Sci.*, 69, 1250–1266, doi:10.1175/JAS-D-11-0165.1, 2012. 18858
- Petters, M. D. and Kreidenweis, S. M.: A single parameter representation of hygroscopic growth and cloud condensation nucleus activity, *Atmos. Chem. Phys.*, 7, 1961–1971, doi:10.5194/acp-7-1961-2007, 2007. 18859
- Randall, D., Krueger, S., Bretherton, C., Curry, J., Duynkerke, P., Moncrieff, M., Ryan, B., Starr, D., Miller, M., Rossow, W., Tselioudis, G., and Wielicki, B.: Confronting models with data – the GEWEX cloud systems study, *B. Am. Meteorol. Soc.*, 84, 455–469, doi:10.1175/BAMS-84-4-455, 2003. 18861
- Rosenfeld, D., Kaufman, Y. J., and Koren, I.: Switching cloud cover and dynamical regimes from open to closed Benard cells in response to the suppression of precipitation by aerosols, *Atmos. Chem. Phys.*, 6, 2503–2511, doi:10.5194/acp-6-2503-2006, 2006. 18858
- Savic-Jovcic, V. and Stevens, B.: The structure and mesoscale organization of precipitating stratocumulus, *J. Atmos. Sci.*, 65, 1587–1605, doi:10.1175/2007JAS2456.1, 2008. 18857

**Marine cellular
cloudiness and
surface heat fluxes**

J. Kazil et al.

Title Page

Abstract

Introduction

Conclusions

References

Tables

Figures

◀

▶

◀

▶

Back

Close

Full Screen / Esc

Printer-friendly Version

Interactive Discussion



**Marine cellular
cloudiness and
surface heat fluxes**

J. Kazil et al.

Title Page

Abstract

Introduction

Conclusions

References

Tables

Figures

◀

▶

◀

▶

Back

Close

Full Screen / Esc

Printer-friendly Version

Interactive Discussion



Shao, Q. and Randall, D. A.: Closed mesoscale cellular convection driven by cloud-top radiative cooling, *J. Atmos. Sci.*, 53, 2144–2165, doi:10.1175/1520-0469(1996)053<2144:CMCCDB>2.0.CO;2, 1996. 18857

Sharon, T. M., Albrecht, B. A., Jonsson, H. H., Minnis, P., Khaiyer, M. M., van Reken, T. M., Seinfeld, J., and Flagan, R.: Aerosol and cloud microphysical characteristics of rifts and gradients in maritime stratocumulus clouds, *J. Atmos. Sci.*, 63, 983–997, doi:10.1175/JAS3667.1, 2006. 18857

Skamarock, W. C., Klemp, J. B., Dudhia, J., Gill, D. O., Barker, D. M., Duda, M. G., Huang, X.-Y., Wang, W., and Powers, J. G.: A Description of the Advanced Research WRF Version 3, Tech. Rep. NCAR/TN-475+STR, National Center for Atmospheric Research, Boulder, CO, USA, 2008. 18859, 18860

Stevens, B., Vali, G., Comstock, K., Wood, R., Van Zanten, M. C., Austin, P. H., Bretherton, C. S., and Lenschow, D. H.: Pockets of open cells and drizzle in marine stratocumulus, *B. Am. Meteorol. Soc.*, 86, 51–57, doi:10.1175/BAMS-86-1-51, 2005. 18857, 18858, 18866

Van Zanten, M. C. and Stevens, B.: Observations of the structure of heavily precipitating marine stratocumulus, *J. Atmos. Sci.*, 62, 4327–4342, doi:10.1175/JAS3611.1, 2005. 18857

Wang, H. and Feingold, G.: Modeling mesoscale cellular structures and drizzle in marine stratocumulus, Part 1: Impact of drizzle on the formation and evolution of open cells, *J. Atmos. Sci.*, 66, 3237–3256, doi:10.1175/2009JAS3022.1, 2009a. 18857, 18858, 18861

Wang, H. and Feingold, G.: Modeling mesoscale cellular structures and drizzle in marine stratocumulus, Part 2: The microphysics and dynamics of the boundary region between open and closed cells, *J. Atmos. Sci.*, 66, 3257–3275, doi:10.1175/2009JAS3120.1, 2009b. 18858, 18861

Wang, H., Feingold, G., Wood, R., and Kazil, J.: Modelling microphysical and meteorological controls on precipitation and cloud cellular structures in Southeast Pacific stratocumulus, *Atmos. Chem. Phys.*, 10, 6347–6362, doi:10.5194/acp-10-6347-2010, 2010. 18858, 18861, 18874

Wood, R.: Stratocumulus clouds, *Mon. Weather Rev.*, 140, 2373–2423, doi:10.1175/MWR-D-11-00121.1, 2012. 18857

Wood, R., Bretherton, C. S., Leon, D., Clarke, A. D., Zuidema, P., Allen, G., and Coe, H.: An aircraft case study of the spatial transition from closed to open mesoscale cellular convection over the Southeast Pacific, *Atmos. Chem. Phys.*, 11, 2341–2370, doi:10.5194/acp-11-2341-2011, 2011. 18857, 18858, 18866, 18867

Xue, H., Feingold, G., and Stevens, B.: Aerosol effects on clouds, precipitation, and the organization of shallow cumulus convection, *J. Atmos. Sci.*, 65, 392–406, doi:10.1175/2007JAS2428.1, 2008. 18857

ACPD

13, 18855–18904, 2013

**Marine cellular
cloudiness and
surface heat fluxes**

J. Kazil et al.

Title Page

Abstract

Introduction

Conclusions

References

Tables

Figures



Back

Close

Full Screen / Esc

Printer-friendly Version

Interactive Discussion



Marine cellular cloudiness and surface heat fluxes

J. Kazil et al.

Title Page

Abstract

Introduction

Conclusions

References

Tables

Figures

◀

▶

◀

▶

Back

Close

Full Screen / Esc

Printer-friendly Version

Interactive Discussion



Table 1. List of simulations. Closed and open bullets represent the closed- and open-cell character of the simulations. The setup of the simulations is identical in all aspects other than those listed here. In simulations with prescribed surface fluxes, the fluxes are spatially homogenized.

Simulation	initial aerosol concentration (mg^{-1})			surface flux		
	Aitken	accumulation	coarse	sensible heat	latent heat	sea salt
S_{\bullet}	0	300	0	interactive	interactive	interactive
S_{\circ}	0	100	0	interactive	interactive	interactive
$S_{\bullet\oplus}$	0	100	0	S_{\bullet}	S_{\bullet}	S_{\bullet}
S_{\circ}^{\prime}	0	100	0	interactive	interactive	0
S_{\bullet}^{\prime}	0	100	0	S_{\circ}	S_{\circ}	S_{\circ}
S_{\circ}^{\prime}	0	300	0	S_{\bullet}	S_{\bullet}	S_{\bullet}
S_{\bullet}^{\prime}	0	100	0	S_{\circ}	S_{\circ}	S_{\circ}

Marine cellular
cloudiness and
surface heat fluxes

J. Kazil et al.

Table 2. Lagged spatial correlation coefficients of surface quantities in simulation S_0 . Correlation coefficients with an absolute value ≥ 0.66 are highlighted. Correlation coefficients in parentheses were calculated from data after filtering with a circular low-pass filter with a diameter of 4500 m. Autocorrelation coefficients for lags < 0 were not calculated. Correlation coefficients between the surface heat fluxes and surface wind speeds were not computed for lags < 0 , because surface heat fluxes are calculated from the simultaneous (total) wind speed at the lowest model level.

		$t = 11 \text{ Jul } 2001 \text{ 21:00:00 UT}$				$t = 12 \text{ Jul } 2001 \text{ 06:00:00 UT}$				
		Time (min)	Temperature	Water vapor	Sensible heat flux	Latent heat flux	Temperature	Water vapor	Sensible heat flux	Latent heat flux
(a)	Residual wind speed	$t - 60$	-0.10 (-0.18)	-0.12 (-0.18)			-0.12 (-0.21)	-0.05 (-0.06)		
		$t - 50$	-0.17 (-0.26)	-0.09 (-0.12)			-0.18 (-0.29)	-0.02 (0.00)		
		$t - 40$	-0.22 (-0.33)	-0.05 (-0.03)			-0.23 (-0.35)	0.02 (0.08)		
		$t - 30$	-0.28 (-0.40)	0.03 (0.10)			-0.30 (-0.45)	0.09 (0.22)		
		$t - 20$	-0.36 (-0.50)	0.15 (0.29)			-0.41 (-0.59)	0.22 (0.42)		
		$t - 10$	-0.49 (-0.63)	0.35 (0.54)			-0.53 (-0.69)	0.39 (0.61)		
		t	-0.62(-0.69)	0.60 (0.70)	0.71 (0.74)	0.51 (0.48)	-0.64 (-0.72)	0.60 (0.72)	0.70 (0.75)	0.47 (0.45)
(b)	Total wind speed	$t - 60$	-0.10 (-0.16)	-0.07 (-0.11)			-0.13 (-0.20)	0.00 (0.01)		
		$t - 50$	-0.15 (-0.22)	-0.04 (-0.05)			-0.16 (-0.23)	0.02 (0.05)		
		$t - 40$	-0.19 (-0.28)	0.01 (0.04)			-0.19 (-0.27)	0.05 (0.11)		
		$t - 30$	-0.23 (-0.33)	0.06 (0.13)			-0.23 (-0.33)	0.10 (0.19)		
		$t - 20$	-0.27 (-0.37)	0.14 (0.25)			-0.29 (-0.40)	0.17 (0.29)		
		$t - 10$	-0.34 (-0.42)	0.26 (0.38)			-0.36 (-0.46)	0.26 (0.40)		
		t	-0.41 (-0.43)	0.40 (0.46)	0.71 (0.69)	0.84 (0.85)	-0.42 (-0.47)	0.38 (0.45)	0.69 (0.69)	0.83 (0.85)
(c)	Temperature	$t - 60$		0.23 (0.28)	0.01 (-0.02)	-0.07 (-0.11)		0.12 (0.12)	-0.07 (-0.13)	-0.12 (-0.20)
		$t - 50$		0.16 (0.17)	-0.08 (-0.14)	-0.11 (-0.17)		0.04 (0.00)	-0.17 (-0.26)	-0.16 (-0.26)
		$t - 40$		0.05 (0.02)	-0.19 (-0.29)	-0.15 (-0.23)		-0.07 (-0.16)	-0.29 (-0.41)	-0.20 (-0.31)
		$t - 30$		-0.08 (-0.16)	-0.33 (-0.45)	-0.21 (-0.30)		-0.21 (-0.35)	-0.43 (-0.58)	-0.25 (-0.37)
		$t - 20$		-0.26 (-0.38)	-0.51 (-0.64)	-0.26 (-0.37)		-0.36 (-0.53)	-0.59(-0.75)	-0.31 (-0.44)
		$t - 10$		-0.48 (-0.61)	-0.71(-0.84)	-0.33 (-0.44)		-0.53(-0.69)	(-0.76) (-0.88)	-0.38 (-0.50)
		t	1 (1)	-0.70 (-0.73)	-0.92(-0.94)	-0.42 (-0.48)	1 (1)	-0.71 (-0.77)	-0.94 (-0.96)	-0.45 (-0.53)
(d)	Water vapor	$t - 60$			0.17 (0.26)	0.11 (0.20)		-0.30 (-0.43)	0.24 (0.37)	0.14 (0.26)
		$t - 50$			0.22 (0.33)	0.13 (0.22)		-0.34 (-0.48)	0.28 (0.42)	0.14 (0.25)
		$t - 40$			0.27 (0.39)	0.13 (0.21)		-0.40 (-0.55)	0.33 (0.48)	0.14 (0.24)
		$t - 30$			0.34 (0.48)	0.13 (0.20)		-0.47 (-0.62)	0.40 (0.55)	0.13 (0.22)
		$t - 20$			0.44 (0.59)	0.11 (0.18)		-0.56 (-0.71)	0.49 (0.65)	0.12 (0.21)
		$t - 10$			0.56 (0.69)	0.09 (0.16)		-0.63(-0.76)	0.58 (0.72)	0.09 (0.19)
		t	-0.70 (-0.73)	1 (1)	0.66 (0.72)	0.04 (0.14)	-0.71 (-0.77)	1 (1)	0.67 (0.74)	0.03 (0.17)

Title Page

Abstract

Introduction

Conclusions

References

Tables

Figures

◀

▶

◀

▶

Back

Close

Full Screen / Esc

Printer-friendly Version

Interactive Discussion



Marine cellular cloudiness and surface heat fluxes

J. Kazil et al.

Title Page

Abstract

Introduction

Conclusions

References

Tables

Figures

◀

▶

◀

▶

Back

Close

Full Screen / Esc

Printer-friendly Version

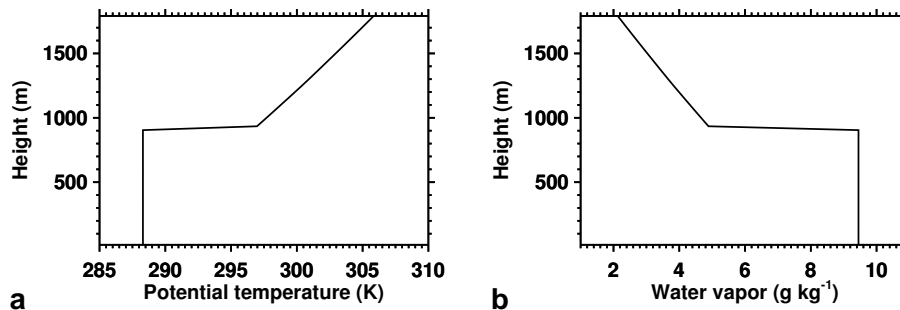
Interactive Discussion

Table 3. Lagged spatial correlation coefficients of surface quantities and vertically integrated cloud properties in simulation \mathcal{S}_s . Correlation coefficients with an absolute value ≥ 0.66 are highlighted. Correlation coefficients in parentheses were calculated from data after filtering with a circular low-pass filter with a diameter of 4500 m.

	Time (min)	$t = 11 \text{ Jul } 2001 \text{ 21:00:00 UT}$				$t = 12 \text{ Jul } 2001 \text{ 06:00:00 UT}$				
		Temperature	Water vapor	Sensible heat flux	Latent heat flux	Temperature	Water vapor	Sensible heat flux	Latent heat flux	
(a)	Latent heat release path	$t - 60$	-0.20 (-0.58)	0.03 (0.16)	0.15 (0.49)	0.08 (0.30)	-0.22 (-0.65)	0.06 (0.29)	0.18 (0.58)	0.10 (0.38)
		$t - 50$	-0.24(-0.66)	0.05 (0.25)	0.19 (0.58)	0.10 (0.35)	-0.27(-0.72)	0.09 (0.35)	0.22 (0.65)	0.11 (0.42)
		$t - 40$	-0.28(-0.71)	0.08 (0.32)	0.22 (0.65)	0.11 (0.39)	-0.29(-0.74)	0.10 (0.40)	0.24 (0.70)	0.13 (0.45)
		$t - 30$	-0.29(-0.70)	0.10 (0.36)	0.25 (0.66)	0.14 (0.41)	-0.30(-0.72)	0.11 (0.43)	0.26 (0.69)	0.15 (0.45)
		$t - 20$	-0.26(-0.61)	0.12 (0.39)	0.24 (0.59)	0.14 (0.35)	-0.27 (-0.65)	0.13 (0.45)	0.25 (0.64)	0.15 (0.41)
		$t - 10$	-0.20 (-0.48)	0.14 (0.39)	0.20 (0.48)	0.11 (0.26)	-0.23 (-0.55)	0.15 (0.44)	0.22 (0.55)	0.13 (0.34)
		t	-0.12 (-0.33)	0.15 (0.37)	0.11 (0.34)	0.01 (0.16)	-0.15 (-0.42)	0.17 (0.41)	0.15 (0.43)	0.05 (0.24)
(b)	Cloud optical depth	$t - 60$	-0.26 (-0.49)	-0.03 (0.02)	0.19 (0.39)	0.13 (0.30)	-0.30 (-0.56)	0.04 (0.17)	0.24 (0.49)	0.16 (0.37)
		$t - 50$	-0.34 (-0.61)	0.02 (0.13)	0.26 (0.52)	0.16 (0.35)	-0.38(-0.68)	0.09 (0.28)	0.31 (0.61)	0.19 (0.42)
		$t - 40$	-0.43(-0.71)	0.08 (0.24)	0.34 (0.63)	0.19 (0.41)	-0.46(-0.76)	0.14 (0.36)	0.38 (0.70)	0.22 (0.47)
		$t - 30$	-0.48(-0.76)	0.13 (0.32)	0.40 (0.69)	0.23 (0.44)	-0.51(-0.80)	0.18 (0.43)	0.44 (0.75)	0.25 (0.49)
		$t - 20$	-0.48(-0.74)	0.17 (0.39)	0.42 (0.70)	0.25 (0.42)	-0.52(-0.79)	0.21 (0.48)	0.46 (0.75)	0.26 (0.48)
		$t - 10$	-0.44(-0.67)	0.22 (0.43)	0.40 (0.64)	0.22 (0.37)	-0.50(-0.74)	0.25 (0.50)	0.45 (0.72)	0.26 (0.45)
		t	-0.36 (-0.56)	0.24 (0.43)	0.33 (0.55)	0.15 (0.29)	-0.42 (-0.65)	0.27 (0.50)	0.39 (0.64)	0.21 (0.38)
(c)	Liquid water path	$t - 60$	-0.23 (-0.41)	-0.06 (-0.03)	0.16 (0.32)	0.14 (0.26)	-0.27 (-0.49)	0.01 (0.12)	0.21 (0.42)	0.16 (0.34)
		$t - 50$	-0.33 (-0.55)	0.00 (0.08)	0.25 (0.45)	0.17 (0.32)	-0.37 (-0.63)	0.08 (0.24)	0.30 (0.56)	0.19 (0.39)
		$t - 40$	-0.43(-0.66)	0.07 (0.20)	0.34 (0.58)	0.20 (0.37)	-0.47(-0.73)	0.14 (0.34)	0.39 (0.66)	0.23 (0.44)
		$t - 30$	-0.51(-0.74)	0.13 (0.29)	0.41 (0.66)	0.23 (0.40)	-0.54(-0.79)	0.18 (0.41)	0.45 (0.73)	0.25 (0.47)
		$t - 20$	-0.55(-0.75)	0.18 (0.36)	0.46 (0.69)	0.25 (0.40)	-0.57(-0.80)	0.21 (0.46)	0.49 (0.76)	0.27 (0.48)
		$t - 10$	-0.53(-0.72)	0.22 (0.40)	0.45 (0.67)	0.23 (0.37)	-0.55(-0.76)	0.25 (0.48)	0.49 (0.73)	0.27 (0.45)
		t	-0.45(-0.62)	0.25 (0.42)	0.40 (0.59)	0.18 (0.31)	-0.48(-0.68)	0.27 (0.48)	0.44 (0.66)	0.23 (0.39)
(d)	Cloud water path	$t - 60$	-0.24 (-0.55)	0.01 (0.10)	0.17 (0.45)	0.11 (0.30)	-0.27 (-0.62)	0.07 (0.24)	0.22 (0.55)	0.13 (0.38)
		$t - 50$	-0.29 (-0.63)	0.05 (0.19)	0.22 (0.55)	0.12 (0.35)	-0.33(-0.70)	0.10 (0.32)	0.26 (0.64)	0.14 (0.42)
		$t - 40$	-0.35(-0.71)	0.09 (0.29)	0.28 (0.64)	0.15 (0.40)	-0.37(-0.75)	0.12 (0.38)	0.31 (0.69)	0.17 (0.46)
		$t - 30$	-0.37(-0.72)	0.11 (0.34)	0.32 (0.67)	0.19 (0.44)	-0.38(-0.75)	0.14 (0.43)	0.33 (0.71)	0.19 (0.47)
		$t - 20$	-0.34 (-0.65)	0.14 (0.38)	0.31 (0.63)	0.20 (0.40)	-0.36(-0.70)	0.17 (0.46)	0.33 (0.68)	0.20 (0.44)
		$t - 10$	-0.28 (-0.54)	0.17 (0.40)	0.27 (0.53)	0.16 (0.31)	-0.33 (-0.63)	0.20 (0.47)	0.32 (0.62)	0.20 (0.39)
		t	-0.20 (-0.41)	0.19 (0.40)	0.20 (0.42)	0.09 (0.22)	-0.25 (-0.52)	0.21 (0.46)	0.25 (0.52)	0.13 (0.31)
(e)	Rain water path	$t - 60$	-0.17 (-0.33)	-0.09 (-0.08)	0.12 (0.24)	0.12 (0.23)	-0.22 (-0.41)	-0.02 (0.06)	0.17 (0.35)	0.15 (0.30)
		$t - 50$	-0.27 (-0.47)	-0.03 (0.04)	0.20 (0.38)	0.15 (0.28)	-0.33 (-0.57)	0.05 (0.20)	0.27 (0.50)	0.18 (0.36)
		$t - 40$	-0.38 (-0.60)	0.04 (0.15)	0.29 (0.51)	0.18 (0.33)	-0.43(-0.69)	0.12 (0.30)	0.36 (0.62)	0.21 (0.41)
		$t - 30$	-0.47(-0.69)	0.11 (0.26)	0.37 (0.61)	0.20 (0.36)	-0.51(-0.76)	0.16 (0.38)	0.43 (0.70)	0.23 (0.45)
		$t - 20$	-0.53(-0.73)	0.15 (0.33)	0.43 (0.66)	0.22 (0.37)	-0.55(-0.79)	0.19 (0.43)	0.47 (0.74)	0.25 (0.46)
		$t - 10$	-0.54(-0.72)	0.19 (0.37)	0.45 (0.66)	0.22 (0.37)	-0.55(-0.77)	0.23 (0.46)	0.47 (0.73)	0.25 (0.45)
		t	-0.48 (-0.65)	0.22 (0.40)	0.41 (0.61)	0.19 (0.32)	-0.49(-0.69)	0.25 (0.47)	0.44 (0.67)	0.24 (0.40)

**Marine cellular
cloudiness and
surface heat fluxes**

J. Kazil et al.

**Fig. 1.** Initial potential temperature and total water (as water vapor) profiles.

Marine cellular cloudiness and surface heat fluxes

J. Kazil et al.

Title Page

Abstract

Introduction

Conclusions

References

Tables

Figures

◀

▶

◀

▶

Back

Close

Full Screen / Esc

Printer-friendly Version

Interactive Discussion

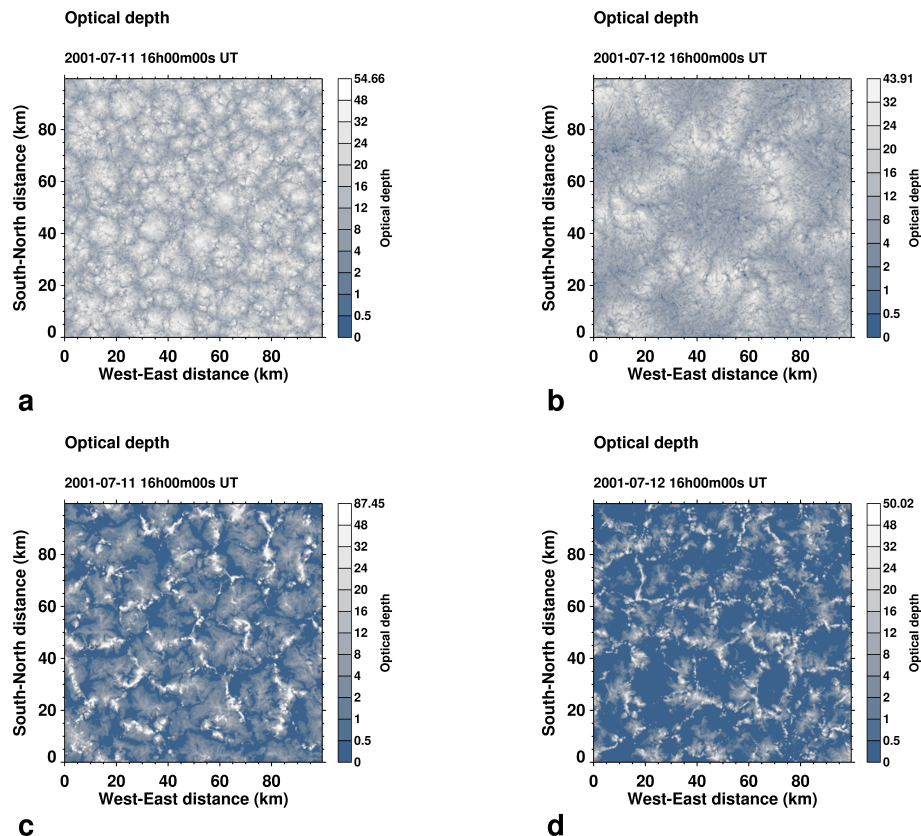


Fig. 2. Cloud optical depth in simulation S_0 (a, b) and S_1 (c, d), after 12 and 36 h. The color scale extends to the cloud optical depth maximum.

Marine cellular
cloudiness and
surface heat fluxes

J. Kazil et al.

Title Page

Abstract

Introduction

Conclusions

References

Tables

Figures

◀

▶

◀

▶

Back

Close

Full Screen / Esc

Printer-friendly Version

Interactive Discussion

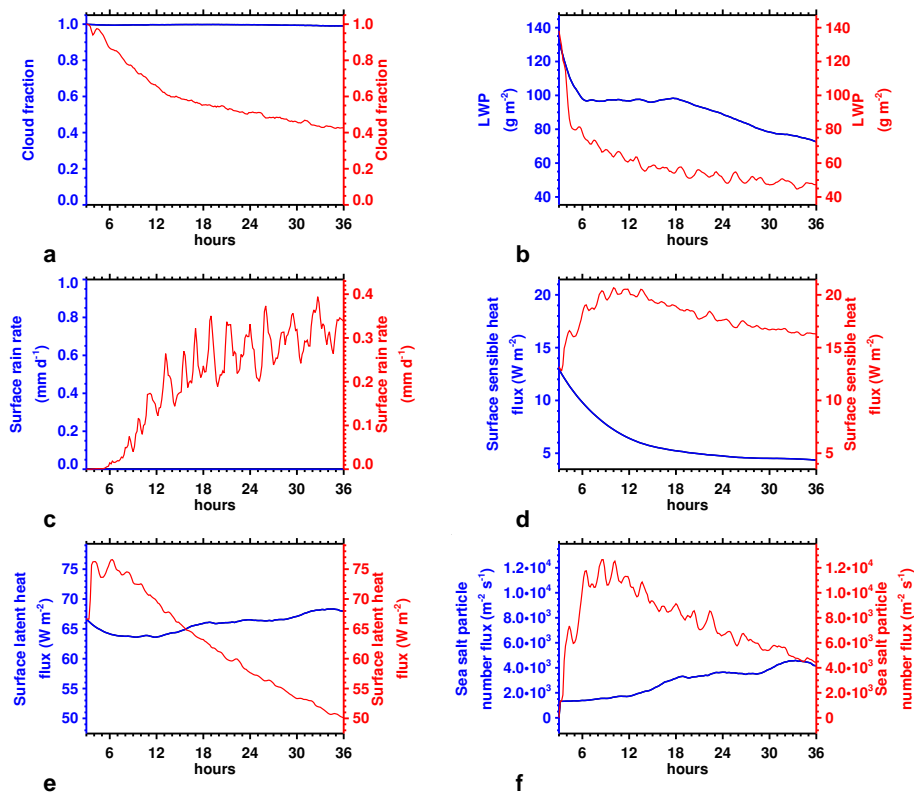


Fig. 3. Domain-averaged time series of selected quantities in simulation S_n (blue) and S_o (red).

Marine cellular
cloudiness and
surface heat fluxes

J. Kazil et al.

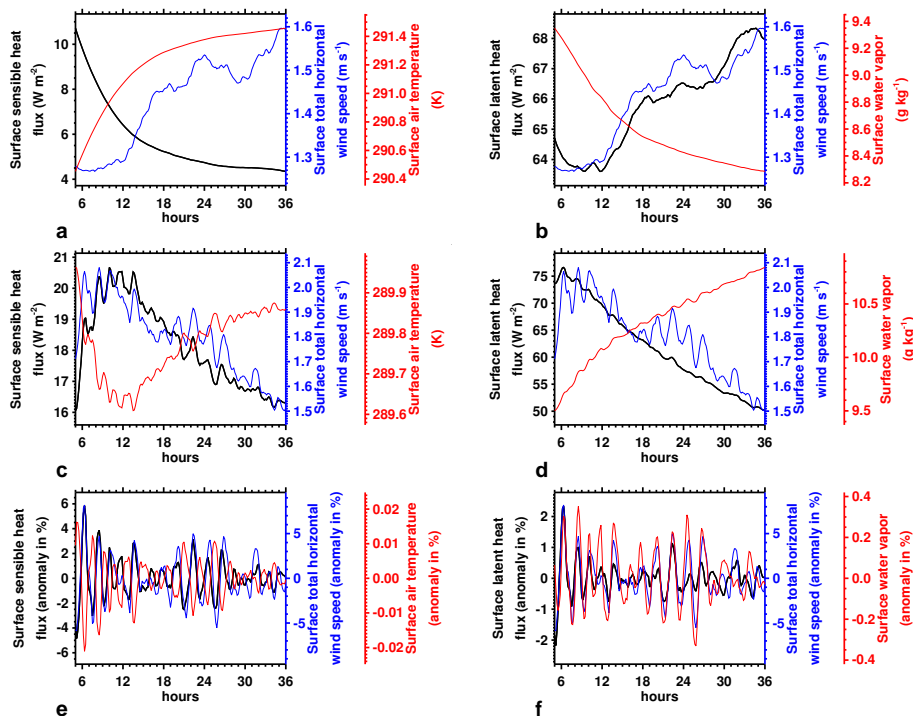


Fig. 4. Domain-averaged surface sensible and latent heat fluxes for the simulation S_1 (**a, b**) and S_0 (**c, d**), plotted with their determinant quantities (domain-averaged surface layer total horizontal wind speed, temperature, and water vapor). (**e, f**) show the temporal anomalies (against a 3 h running mean) of the S_0 data (**c, d**).

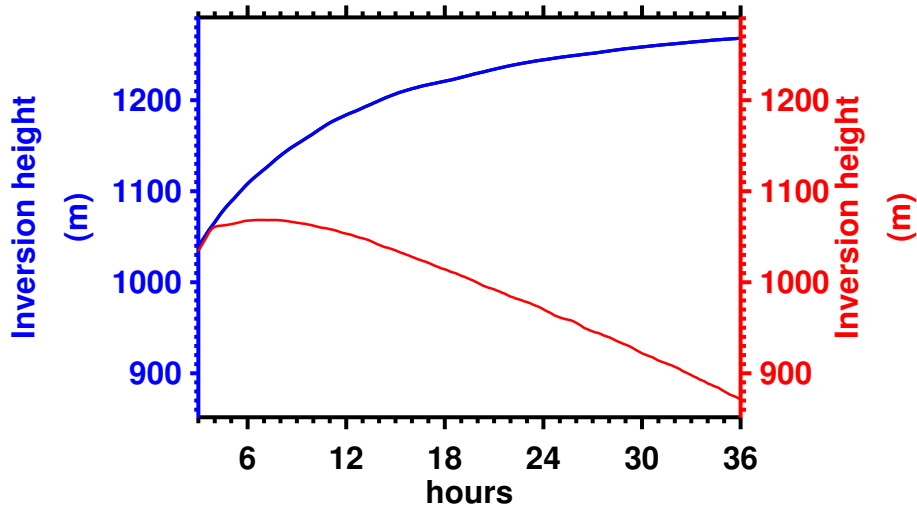


Fig. 5. Domain-averaged inversion height time series in simulation S_0 (blue) and S_0 (red).

Marine cellular cloudiness and surface heat fluxes

J. Kazil et al.

Title Page

Abstract Introduction

Conclusions References

Tables Figures

◀ ▶

◀ ▶

Back Close

Full Screen / Esc

Printer-friendly Version

Interactive Discussion



Marine cellular cloudiness and surface heat fluxes

J. Kazil et al.

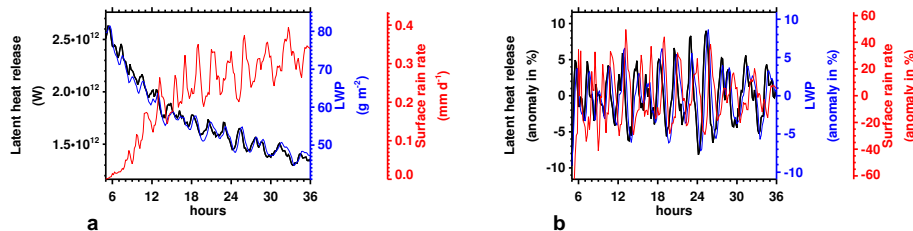


Fig. 6. (a) Domain-integrated latent heat release (heating of the air from condensation of water vapor), domain-averaged liquid water path and surface rain, and (b) their temporal anomalies (against a 3 h running mean) in simulation S_o .

Title Page

Abstract

Introduction

Conclusions

References

Tables

Figures

◀

▶

◀

▶

Back

Close

Full Screen / Esc

Printer-friendly Version

Interactive Discussion



Marine cellular
cloudiness and
surface heat fluxes

J. Kazil et al.

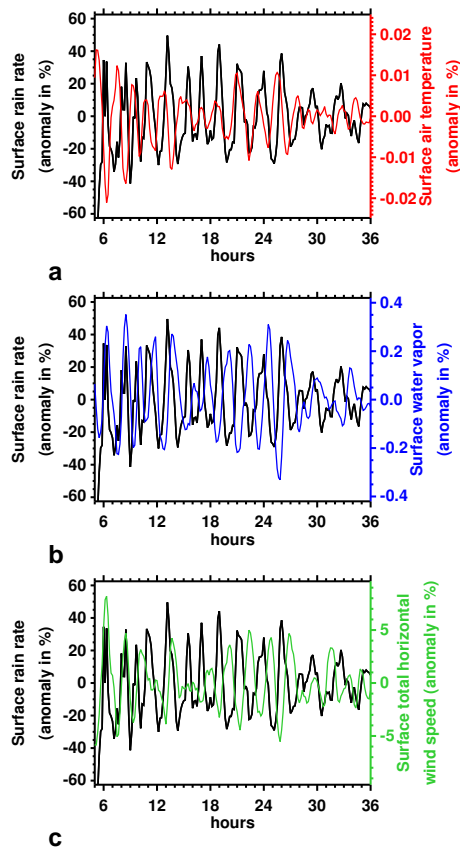


Fig. 7. Temporal anomalies (against a 3 h running mean) of surface rain and **(a)** surface layer temperature, **(b)** water vapor, and **(c)** total horizontal wind speed in simulation \mathcal{S}_c .

[Title Page](#)[Abstract](#)[Introduction](#)[Conclusions](#)[References](#)[Tables](#)[Figures](#)[◀](#)[▶](#)[◀](#)[▶](#)[Back](#)[Close](#)[Full Screen / Esc](#)[Printer-friendly Version](#)[Interactive Discussion](#)

Marine cellular
cloudiness and
surface heat fluxes

J. Kazil et al.

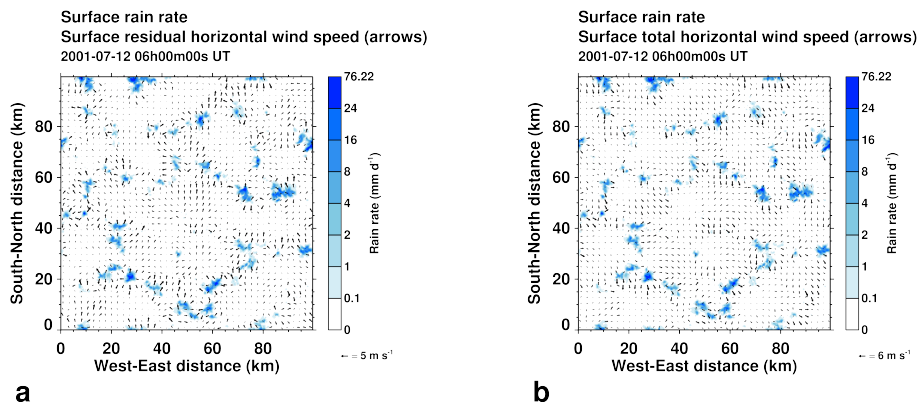


Fig. 8. Surface rain rate with the residual (a) and total (b) horizontal wind speed in simulation S_0 . The color scales are bounded by the minimum and maximum of the data.

Marine cellular cloudiness and surface heat fluxes

J. Kazil et al.

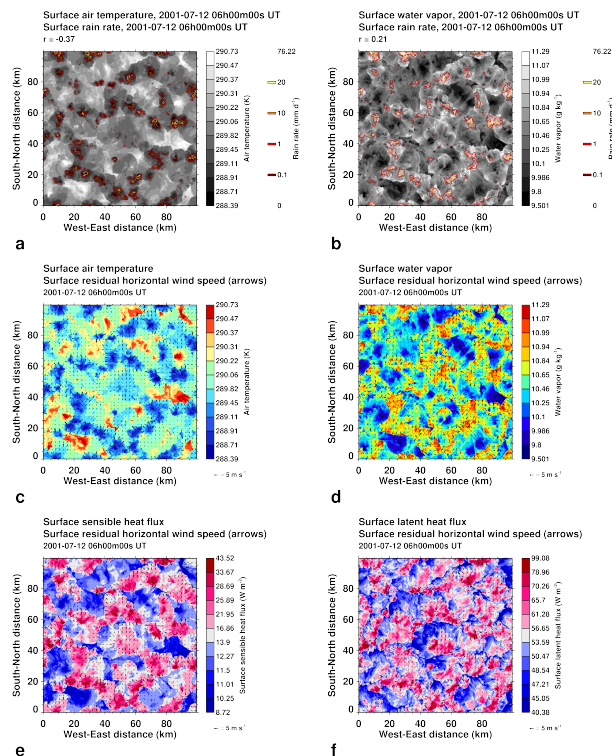


Fig. 9. Surface rain rate with surface air temperature (**a**) and surface water vapor (**b**); surface air temperature (**c**) and water vapor (**d**) with the residual horizontal surface wind field; and the surface sensible (**e**) and latent (**f**) heat flux with the residual horizontal surface wind field, in simulation S_0 . The corresponding spatially filtered data are shown in the Supplement, Fig. A1. The color scales are bounded by the minimum and maximum of the data. Minimum and maximum line contours are suppressed.

Marine cellular
cloudiness and
surface heat fluxes

J. Kazil et al.

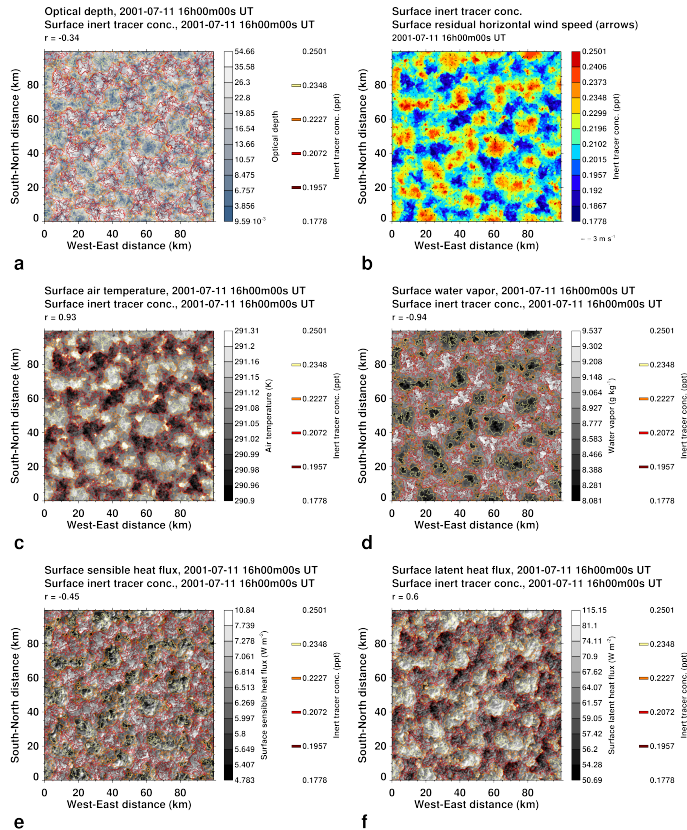


Fig. 10. Surface concentration of the inert tracer, with (a) cloud optical depth, (b) residual horizontal surface wind field, (c) surface air temperature, (d) surface water vapor, and surface sensible (e) and latent (f) heat flux, in simulation S_0 . The corresponding spatially filtered data are shown in the Supplement, Fig. A2. The color scales are bounded by the minimum and maximum of the data. Minimum and maximum line contours are suppressed.

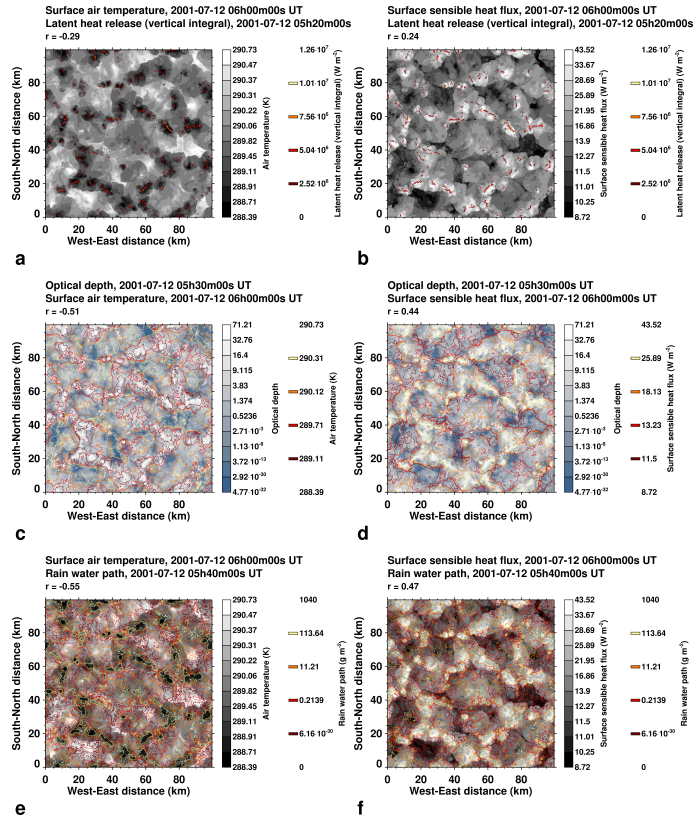


Fig. 11. Lagged correlation of the latent heat release path with **(a)** surface air temperature and **(b)** surface sensible heat flux, of cloud optical depth with **(c)** surface air temperature and **(d)** surface sensible heat flux, and of the rain water path with **(e)** surface air temperature and **(f)** surface sensible heat flux, in simulation S_c . The corresponding spatially filtered data are shown in the Supplement, Fig. A3. The color scales are bounded by the minimum and maximum of the data. Minimum and maximum line contours are suppressed.

[Title Page](#)
[Abstract](#)
[Introduction](#)
[Conclusions](#)
[References](#)
[Tables](#)
[Figures](#)

[Back](#)
[Close](#)
[Full Screen / Esc](#)
[Printer-friendly Version](#)
[Interactive Discussion](#)

Marine cellular
cloudiness and
surface heat fluxes

J. Kazil et al.

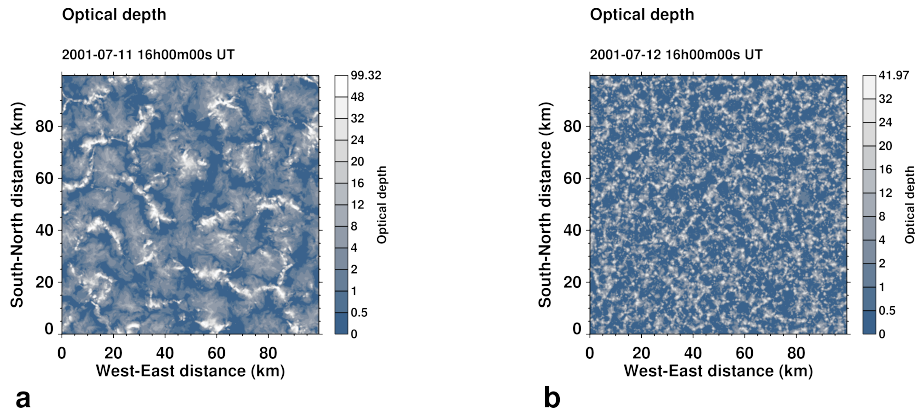


Fig. 12. Cloud optical depth in simulation S_{\otimes} (**a**, **b**) after 12 and 36 h. The color scale extends to the cloud optical depth maximum.

[Title Page](#)[Abstract](#)[Introduction](#)[Conclusions](#)[References](#)[Tables](#)[Figures](#)[⏪](#)[⏩](#)[◀](#)[▶](#)[Back](#)[Close](#)[Full Screen / Esc](#)[Printer-friendly Version](#)[Interactive Discussion](#)

Marine cellular cloudiness and surface heat fluxes

J. Kazil et al.

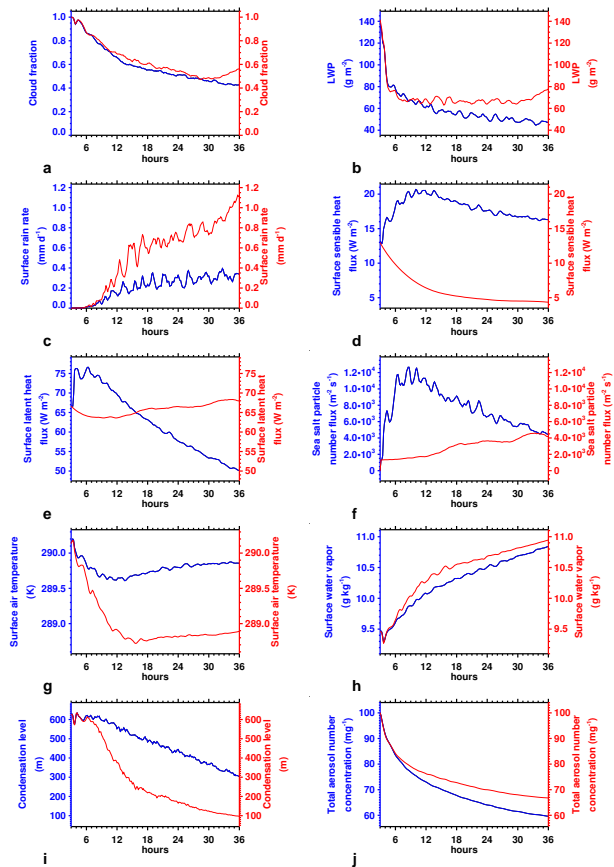


Fig. 13. Domain-averaged time series of selected quantities in simulation S_0 (blue) and S_0^* (red).

Title Page

Abstract Introduction

Conclusions References

Tables Figures

◀ ▶

◀ ▶

Back Close

Full Screen / Esc

Printer-friendly Version

Interactive Discussion



Marine cellular cloudiness and surface heat fluxes

J. Kazil et al.

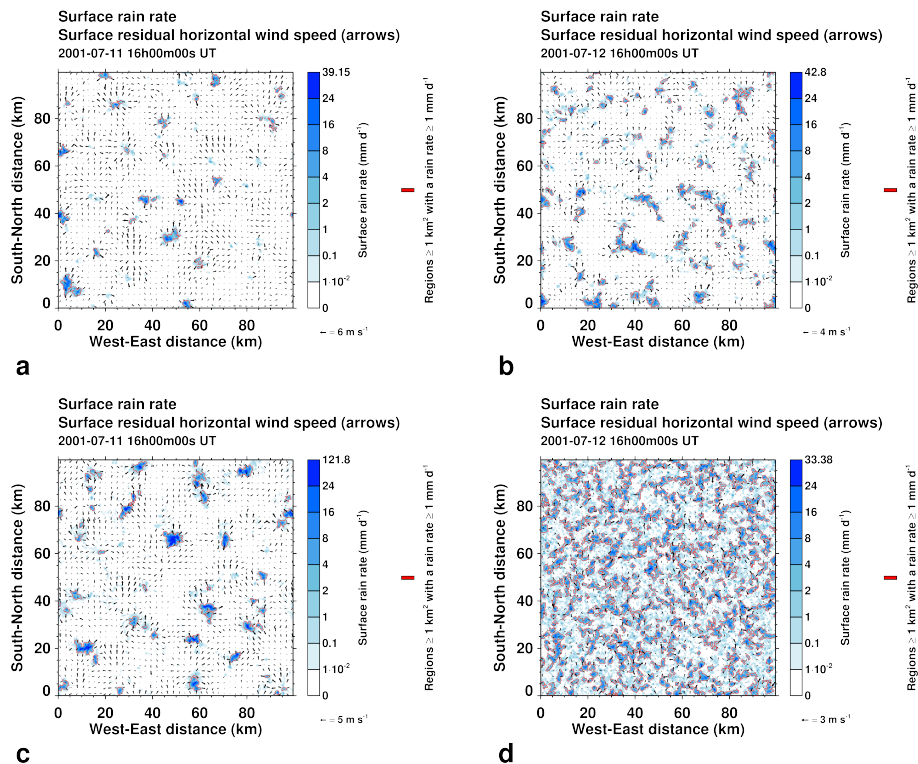


Fig. 14. Rain regions $\geq 1 \text{ km}^2$, with a surface rain rate $\geq 1 \text{ mm d}^{-1}$, at two times in simulation S_0 (**a, b**) and S_8 (**c, d**), with the residual wind speed. The color scales are bounded by the minimum and maximum of the data.

Title Page

Abstract

Introduction

Conclusions

References

Tables

Figures

⏪

⏩

⏴

⏵

Back

Close

Full Screen / Esc

Printer-friendly Version

Interactive Discussion



Marine cellular
cloudiness and
surface heat fluxes

J. Kazil et al.

Title Page

Abstract

Introduction

Conclusions

References

Tables

Figures

◀

▶

◀

▶

Back

Close

Full Screen / Esc

Printer-friendly Version

Interactive Discussion

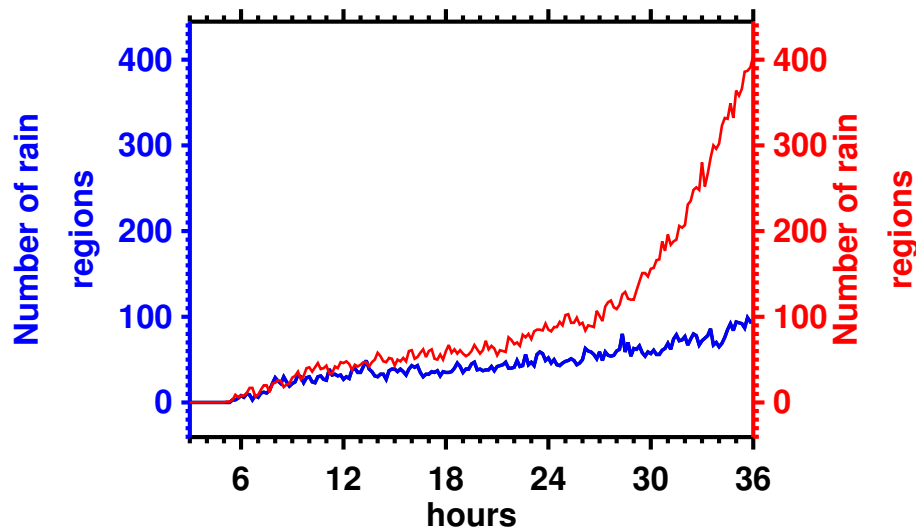


Fig. 15. Temporal evolution of the number of rain regions $\geq 1 \text{ km}^2$, with a surface rain rate $\geq 1 \text{ mm d}^{-1}$, in simulation \mathcal{S}_0 (blue) and \mathcal{S}_∞ (red).

Marine cellular cloudiness and surface heat fluxes

J. Kazil et al.

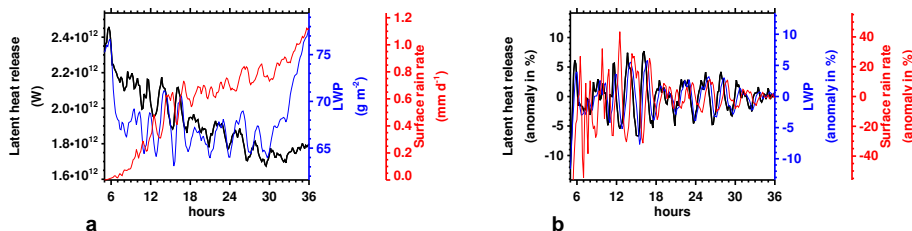


Fig. 16. (a) domain-integrated latent heat release (heating of the air from condensation of water vapor), domain-averaged liquid water path and surface rain, and (b) their temporal anomalies (against a 3 h running mean) in simulation S_{\otimes} .

Title Page

Abstract

Introduction

Conclusions

References

Tables

Figures

◀

▶

◀

▶

Back

Close

Full Screen / Esc

Printer-friendly Version

Interactive Discussion



Marine cellular
cloudiness and
surface heat fluxes

J. Kazil et al.

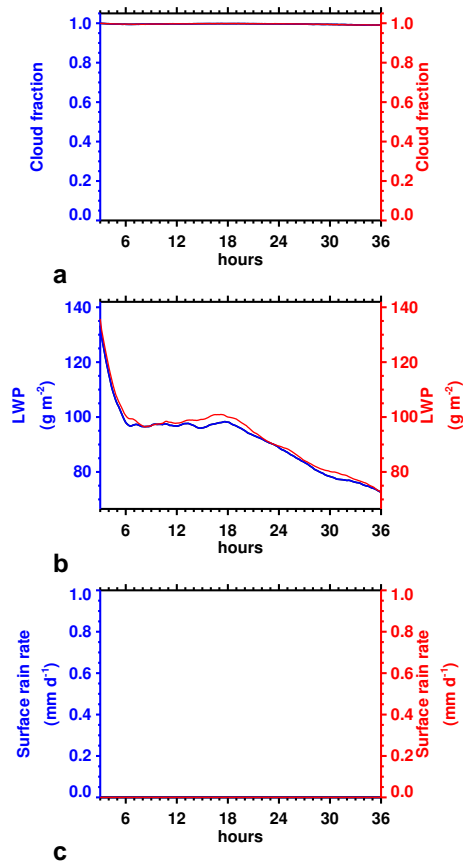


Fig. 17. Domain-averaged time series of selected quantities in simulation S_+ (blue) and S_- (red).

Marine cellular
cloudiness and
surface heat fluxes

J. Kazil et al.

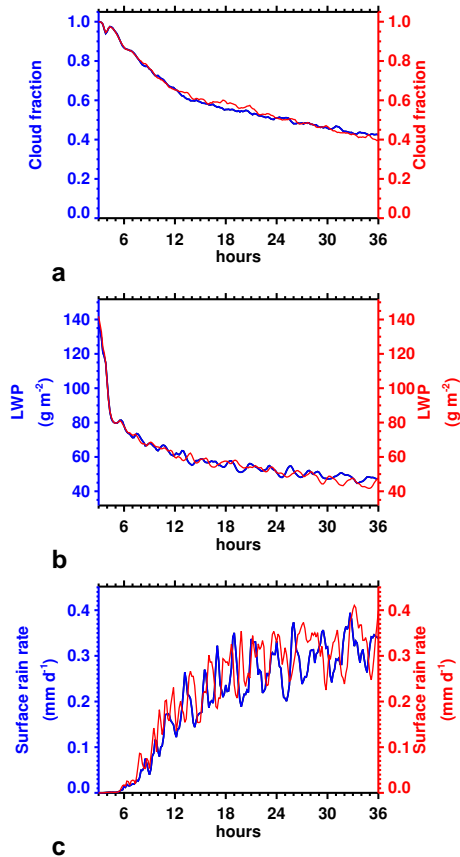


Fig. 18. Domain-averaged time series of selected quantities in simulation S_0 (blue) and S_c (red).

Title Page

Abstract

Introduction

Conclusions

References

Tables

Figures

◀

▶

◀

▶

Back

Close

Full Screen / Esc

Printer-friendly Version

Interactive Discussion

